Influence of Surface Drag on the Evolution of Fronts

KEITH M. HINES AND CARLOS R. MECHOSO

Department of Atmospheric Sciences, University of California at Los Angeles, Los Angeles, California

(Manuscript received 10 February 1992, in final form 10 August 1992)

ABSTRACT

Surface frontal structure during cyclogenesis, and the sensitivity of this structure to surface friction, is examined. The approach is based on the analyses of simulations using a primitive equation model, with the domain restricted to a sector of one hemisphere, and the physics reduced to surface drag, horizontal diffusion, and dry convective adjustment. The model horizontal resolution is 1.2° latitude × 1.5° longitude, and there are 21 layers in the vertical. The drag coefficient is varied in simulations with midlatitude jet streams as initial conditions. The extent to which simulations in the adiabatic framework or with highly simplified representations of physical processes succeed in producing features of cyclone evolution emphasized by recent observational analyses is evaluated.

Shallow bent-back warm fronts develop in simulations with surface drag coefficients that are zero or representative of ocean surfaces. Horizontal advection, first in strong easterly and later in strong northerly winds, is primarily responsible for the resulting bent-back structure of the warm front.

The effect of surface drag on simulated lower-tropospheric wind speeds and frontogenesis is nonuniform. Warm frontogenesis is enhanced in simulations with relatively low surface drag through a feedback process involving vorticity, deformation, convergence, and warm-air advection. Surface drag tends to inhibit warm frontogenesis by decreasing the low-level wind speed and reducing the contribution of warm advection to the feedback. Consistently, a distinct warm front does not develop in the simulation with a surface drag coefficient representative of continental surfaces. Cold frontogenesis, on the other hand, is not very sensitive to surface drag.

Further simulations with doubled horizontal resolution (0.6° latitude × 0.75° longitude), slightly higher baroclinity at lower levels in the initial conditions, and small surface drag produce bent-back fronts that spiral around the surface pressure minimum. These results suggest that there are important differences in the structure of surface fronts associated with marine and continental cyclogenesis.

1. Introduction

In the classical picture [e.g., that provided by the Bergen school—Bjerknes (1919); Bjerknes and Solberg (1921)] cold and warm surface fronts result from the development of an unstable wave on a preexisting frontal surface. Warm and cold fronts "pivot" around their intersection point so as to become nearly parallel and finally coincide during the occlusion process. When occlusion is completed, a cyclonic circulation remains in the cold air. This classical model has been extensively applied to the description of surface frontal evolution.

Recent observational and modeling studies are providing a higher variety of frontal structures. Mass (1991) reviews differences between the classical model and observed cyclones. He proposes several possible changes in methods of analysis for surface frontal zones. Shapiro and Keyser (1990) develop a modified model of frontal development during oceanic cyclogenesis based on the results of observational campaigns.

In this study, we analyze the evolution of warm and cold fronts obtained in simulations of the life cycles of unstable baroclinic waves with a 3D primitive equation (PE) model. The model does not include any diabatic or viscous processes other than dry convective adjustment, horizontal diffusion, and surface friction. The extent to which the recently discovered features in frontal structures can be simulated in the adiabatic framework or with a highly simplified representation of physical processes is addressed.

The approach to investigation herein does not imply ignoring the importance of moist processes on the evolution of frontal structures. The effect of moist physics and low-level heat fluxes on cyclogenesis and frontal zones has been emphasized in many studies (Hsie et al. 1984; Orlanski et al. 1985; Emanuel et al. 1987; Davis and Emanuel 1988; Mullen and Baumhefner 1988; Kuo and Reed 1988; Kuo and Low-Nam 1990; Neiman et al. 1990; and Kuo et al. 1991a,b). Nevertheless, several authors eloquently endorse the need for further studies in the adiabatic framework (Shapiro and Keyser 1990; Kuo et al. 1991b).

We perform detailed analyses of the sensitivity of frontal structure to surface friction. Sanders and

Corresponding author address: Dr. Keith M. Hines, Byrd Polar Research Center, The Ohio State University, 1090 Carmack Road, Columbus, OH 43210-1002.

Gyakum (1980) find that intense cases of rapidly deepening cyclones usually develop over ocean surfaces. Mass (1991) notes that weaker surface friction and larger heat fluxes over water can have major effects on the structural evolution of cyclones, at least in the lower troposphere. He discusses the equatorward-bending occluded fronts that seem to be oceanic features rarely observed over continents. Our analyses address the validity of this hypothesis as far as surface friction is concerned.

Section 2 reviews selected observational and modeling studies of surface frontal evolution. Of particular interest are the effects of surface friction on frontogenesis, and the differences between warm and cold fronts. Section 3 describes the numerical model used. Section 4 presents the comparison of the simulated frontogenesis with differing values of the drag coefficient. Section 5 describes the feedback process found in the simulated frontogenesis. Section 6 presents the interrelations between the surface front and the baroclinic wave in the upper troposphere. Section 7 presents the results of additional simulations with higher horizontal resolution. A summary of the results of this study and the conclusions are given in section 8.

2. Selected observational and modeling studies of surface frontal evolution

a. *Observational studies*

Shapiro and Keyser (1990) present the development of a frontal cyclone through four stages (see their Fig. 10.27). In the first stage, an incipient cyclone wave is located on a broad (roughly 400 km wide) frontal zone. At the second stage, the baroclinic zone has sharpened, forming distinct warm and cold frontal zones. Part of the cold front has "fractured" or weakened near the intersection with the warm front. In the third stage, at roughly the midpoint of cyclogenesis, the cold front has propagated eastward and is roughly perpendicular to the warm front, forming a "T-bone" structure. The western section of the polewardmost front has begun to bend south. Shapiro and Keyser refer to this feature as a "bent-back" warm front, while Kuo et al. (1992) refer to it as an occluded front. In the final stage, there is a warm-core seclusion in the western part of the fully developed cyclone. Temperatures in the seclusion are colder than those within the warm sector. The frontal zone now spirals into the surface low. Elements of this frontogenesis model are found in adiabatic simulations of frontogenesis performed by Mudrick (1974, 1978), Takayabu (1986), and Schär (1989). Bent-back fronts are also found in simulations, including diabatic processes, performed by Shapiro and Keyser (1990), Neiman et al. (1990), and Kuo et al. (1991b, 1992).

Shapiro and Keyser (1990) discuss observational evidence of bent-back fronts in rapidly deepening cyclones. The southward bending occurs in strong northerly or northeasterly winds that decay rapidly with height from intensities of up to 40 m s^{-1} at very low levels. Accordingly, bent-back fronts tend to be a shallow feature. In a particular case, the bent-back front is characterized by a width of 50 km, a depth of 100 mb, a temperature gradient of 10 K $(100\ km)^{-1}$, a cross-front shear of $10^{-3}\ s^{-1}$, and a vertical shear of 40 m s^{-1} $(100\ mb)^{-1}$.

In the pioneering study of frontogenesis (Bjerknes 1919), it is noted that warm fronts are preceded by stratiform clouds, while cold fronts are accompanied by convective clouds. Other studies find that cold fronts are typically steeper and less statically stable than warm fronts (Bergeron 1937; Bannon 1984). Over the oceans, warm fronts are often regions of largest ascent and precipitation (Kuo et al. 1991b). Warm fronts are frequently diffuse phenomena that can be more difficult to locate than cold fronts (Wallace and Hobbs 1977).

b. *Modeling studies*

There are numerous simulations and analyses of surface frontogenesis with 2D models. These analyses have demonstrated that the inclusion of ageostrophic dynamics in a model forced by a deformation field can lead to the formation of discontinuities in the temperature and wind fields within a finite time (e.g., Hoskins and Bretherton 1972, p. 19). It is more difficult to obtain the distinct characteristics of either warm or cold fronts with 2D models (see Williams et al. 1981).

In this regard, Eliassen (1962), Gidel (1978), and Keyser and Pecnick (1987) differentiate between fronts based on the local orientation of the thermal wind to the frontal zone. Gidel (1978) and Keyser and Pecnick (1987) find that horizontal shear forcing can result in stronger fronts if the thermal wind points toward the warm side of the frontal zone (cold-advection case). Keyser and Pecnick (1987) point out that positive feedback results in rapid increases in low-level vorticity and convergence. The growth in these quantities is even more rapid during the early stages of the warm-advection simulation, which has large ascent over the frontal zone. The enhancement of the horizontal temperature gradient in this case is weakened by the frontolytical contribution of horizontal shear.

In the 3D framework, warm and cold fronts at the surface can develop simultaneously. Mudrick's (1974) simulation shows a more intense warm front than cold front. This is apparently due to the contribution of divergence, which is frontogenetical along the warm front and approximately zero along the cold front; although, the contribution of deformation is about three times larger along the warm front. The latter contribution is frontogenetical and of comparable magnitude along both fronts. Further, Hoskins and West (1979) find that the relative intensities of warm and cold fronts in their semigeostrophic simulations are sensitive to the initial horizontal shear. Hoskins and Heckley

(1981) mention that warm and cold fronts are associated with different tilts with height of the temperature wave.

Takayabu (1986) analyzes the role of horizontal advection during 3D simulations of frontogenesis. He uses a dry, primitive equation model initialized with a baroclinic westerly jet stream. The model produces a cold front west of the warm sector and another front, which he does not refer to as a warm front, at the poleward edge of the warm sector. Parcels undergo frontogenesis and frontolysis in the eastern and western sections, respectively, of the latter front due to the combined effect of deformation and divergence. Takayabu (1986) finds that, nevertheless, horizontal advection is responsible for the extension of the frontal zone to the west and south.

Kuo et al. (1992) simulate the development of the *Ocean Ranger* storm of October 1982. At the mature stage of the cyclone, the strongest temperature gradients are located along the occluded front. Their trajectory analysis reveals that, in the development of the seclusion, colder air isolates the warmer air by rotating around the surface low.

c. *Effect of surface friction*

It has been found that Ekman-layer processes reduce linear baroclinic instability (Haltiner and Caverly 1965; Card and Barcilon 1982; Farrell 1985; Valdes and Hoskins 1988). Frictional processes are expected, therefore, to influence the characteristics of frontogenesis in the lower troposphere during the evolution of cyclones. This expectation is confirmed by results obtained in 2D simulations. Williams (1974) finds that inclusion of an Ekman layer prevents the formation of discontinuities in the flow. After a few days of simulation, an approximate balance is established between frontogenetical processes and dissipation. Keyser and Anthes (1982) find that inclusion of a planetary boundary layer allows for a more realistic simulation, including a narrow updraft at low levels on the warm edge of the frontal zone. Levy (1989) studies the impact of boundary-layer processes on frontogenesis. Based on a combination of observations, modeling results, and theoretical considerations, he suggests that boundary-layer flow is more favorable for cold frontogenesis than warm frontogenesis.

Weak lower-tropospheric fronts are obtained in the 3D simulations performed by Fischer (1977). His results suggest that surface friction has different effects on warm and cold fronts. In particular, some surface drag parameterizations produce more intense cold fronts than warm fronts.

There are 3D simulations that specifically mention the impact of surface drag on rapidly developing cyclones over the oceans. Kuo and Reed (1988) use the Pennsylvania State University–National Center for Atmospheric Research (PSU–NCAR) Mesoscale Model. They find that removal of surface friction in a dry simulation increases the deepening of the surface low by 5–7 mb in a 24-h period. Mullen and Baumhefner (1988) use the NCAR Community Climate Model (CCM) to compare simulations performed by using surface drag coefficients representative of ocean and land surfaces. They conclude that the larger surface drag, smaller surface heat fluxes, and the reduced precipitation over land appear as three primary reasons for the lack of explosive cyclogenesis over the continents in their simulations.

In summary, recent analyses of observational data have revealed different characteristics in the cyclones developing over oceans and continents. Shapiro and Keyser's (1990) revised model of cyclone evolution over the oceans includes the formation of a bent-back front, which can eventually spiral about the surface pressure minimum. Further, studies with 2D and 3D models have examined differences between cold and warm frontogenesis. Idealized simulations often produce strong warm fronts, which are infrequently observed over land. The weakness of warm frontogenesis over land has been attributed to the effect of boundary-layer processes.

3. Description of the model

The prognostic variables of the model are horizontal velocity, potential temperature, and surface pressure. In the horizontal, the model's equations are discretized using a staggered longitude–latitude C grid (Arakawa and Lamb 1977). The treatment of the horizontal-advection terms in the momentum equation is based on the potential enstrophy–conserving scheme (Arakawa and Lamb 1981) modified to give fourth-order accuracy for the advection of potential vorticity. The horizontal-advection scheme used for the potential temperature is also fourth order and conserves the global mass integral of its square. In the vertical, the model uses a modified σ-coordinate system in which the lower boundary and isobaric surfaces above 100 mb are coordinate surfaces. The distribution of model variables in the vertical is shown in Fig. 1. This distribution cor-

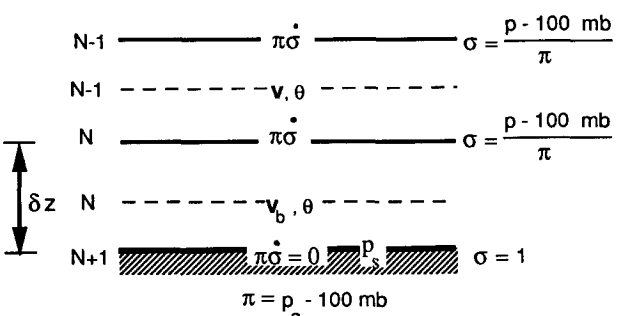

FIG. 1. Vertical distribution of variables in the lowest two layers of the N-layer model; θ is potential temperature, P_s is surface pressure, and $\dot{\sigma}$ is vertical velocity.

responds to a Lorenz-type grid (Lorenz 1960). The physical parameterizations are reduced to dry convective adjustment, horizontal diffusion, and surface drag. The diffusion is by a nonlinear "eddy viscosity" of the type used by Manabe et al. (1970), but with an order-of-magnitude smaller coefficient. The surface stress τ is obtained by using the bulk aerodynamic formula,

$$\tau = \rho C_D |\mathbf{v}_b| \mathbf{v}_b, \tag{1}$$

where $\mathbf{v}_b$ is the horizontal velocity at the lowest layer of the model, ρ is density, and C_D is the surface drag coefficient. The effect of surface drag is incorporated into the momentum equation as a deceleration given by

$$\left.\frac{d\mathbf{v}_b}{dt}\right|_r = -\frac{1}{\rho}\frac{\tau}{\delta \bar{z}}, \tag{2}$$

where t is time, and $\delta \bar{z}$ is a constant average value for the depth of the lowest layer.

The model domain is a sector comprising one-sixth of a hemisphere with periodic boundary conditions in longitude and a symmetry condition at the equator. The horizontal scale of motions in the 60° sector domain of the model corresponds well with the roughly 4500-km east–west scale of the cloud system displayed in Fig. 10.22 of the observational study by Shapiro and Keyser (1990). All prognostic variables are symmetric about the equator, except for the meridional velocity component that is antisymmetric about the equator. No orographic elevations are included in the boundary conditions. The top of the model, at 1 mb, is assumed to be a material surface. This simplified version of the UCLA General Circulation Model (GCM) has been used in studies of upper-level frontogenesis (Hines and Mechoso 1991).

The standard resolution for the integrations performed for this study is 1.2° latitude × 1.5° longitude. Higher horizontal resolution is double the standard resolution (0.6° latitude × 0.75° longitude). In all cases, there are 21 levels in the vertical, with 7 levels above 100 mb.

The initial conditions for the simulations are shown in Fig. 2. They consist of a zonally symmetric jet stream, which is given by

$$\bar{u}(\phi, p) = \hat{u}(p) \sin(\pi \sin^2\phi), \tag{3}$$

where ϕ is the latitude, p is pressure, and $\hat{u}(p)$ corresponds to winter-mean conditions at 45°N (Oort 1983). Maximum wind speed is 39.8 m s^{-1} at 45° latitude, 200 mb. The wind is zero at the surface, and sea level pressure is a constant 1000 mb. The initial temperature distribution is found from (3) under the assumption of gradient balance and the application of a reference temperature profile in the vertical corresponding to winter-mean conditions (Oort 1983) at 34°N.

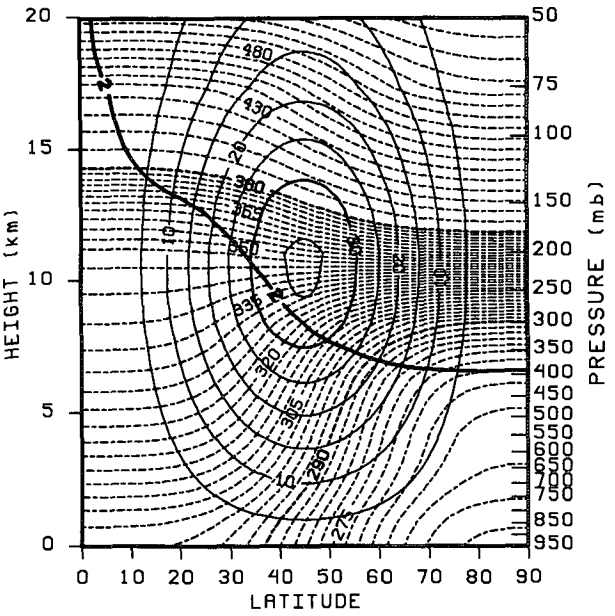

FIG. 2. Latitude–height contour plot of the zonal wind velocity (m s^{-1}, solid lines) given by Eq. (3) and the corresponding potential-temperature distribution (K, dashed lines). The contour interval for wind velocity is 5 m s^{-1}; the thick, solid contour is 30 m s^{-1}. The contour interval for potential temperature is 3 K and 10 K above and below 380 K, respectively. Thick dashed contours are 290 and 380 K.

In the initial 3-day period of all simulations, the zonally independent component of all prognostic fields is held constant in time, and all wave components other than the longest component consistent with the sector are filtered out. Following this procedure reduces small-scale features of the flow as the perturbation organizes into the most unstable structure of the linear system. The origin of time in the discussion below corresponds to the end of such a "linear" stage.

4. Results from the simulations

To evaluate the effects of surface drag on frontogenesis in the lower troposphere, a series of simulations are performed with drag coefficient values $C_D = 0, 0.56 \times 10^{-3}$, and 2.0×10^{-3} [see Eq. (1)]. The latter two correspond to a neutral boundary layer with characteristic roughness lengths of 2×10^{-4} and 2×10^{-1} m, according to

$$C_D = \left[\frac{0.35}{\ln(z/z_0)}\right]^2, \tag{4}$$

where $z = 508$ m, and z_0 is the roughness length. The simulations with drag coefficients equal to 0, 0.56×10^{-3}, and 2.0×10^{-3} will hereby be referred to as no drag, ocean drag, and land drag, respectively.

Figures 3, 4, and 5 display surface pressure and potential temperature at the model's lowest level ($\sigma = 0.936$) during the evolution of the unstable flow in

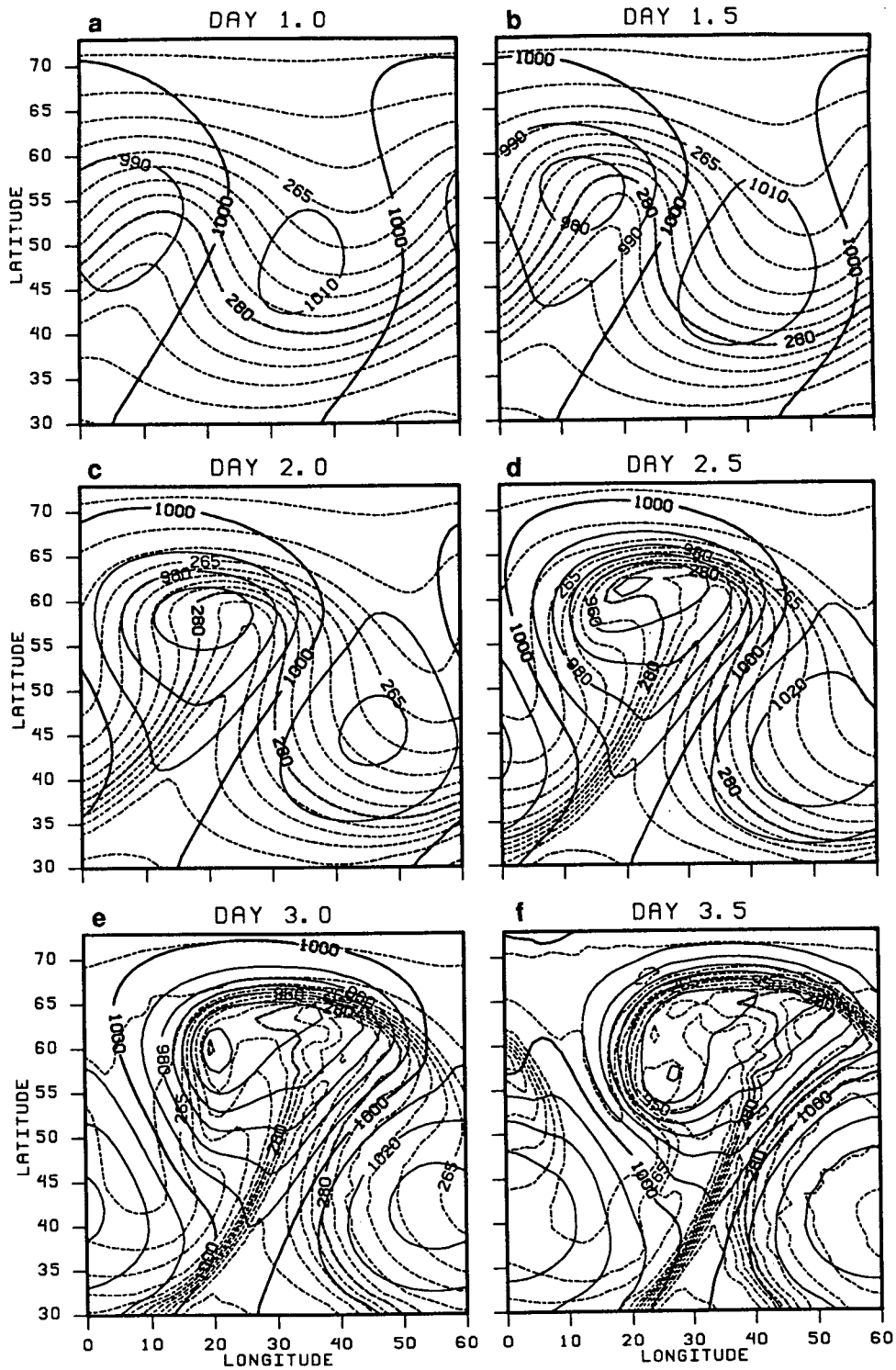

FIG. 3. Longitude–latitude contour plot of surface pressure (mb, solid lines) and model's lowest-level potential temperature (K, dashed lines) for no drag at (a) day 1.0, (b) day 1.5, (c) day 2.0, (d) day 2.5, (e) day 3.0, and (f) day 3.5. The contour interval for surface pressure is 10 mb; the thick, solid line is 1000 mb. The contour interval for potential temperature is 3 K; the thick dashed contour is 280 K.

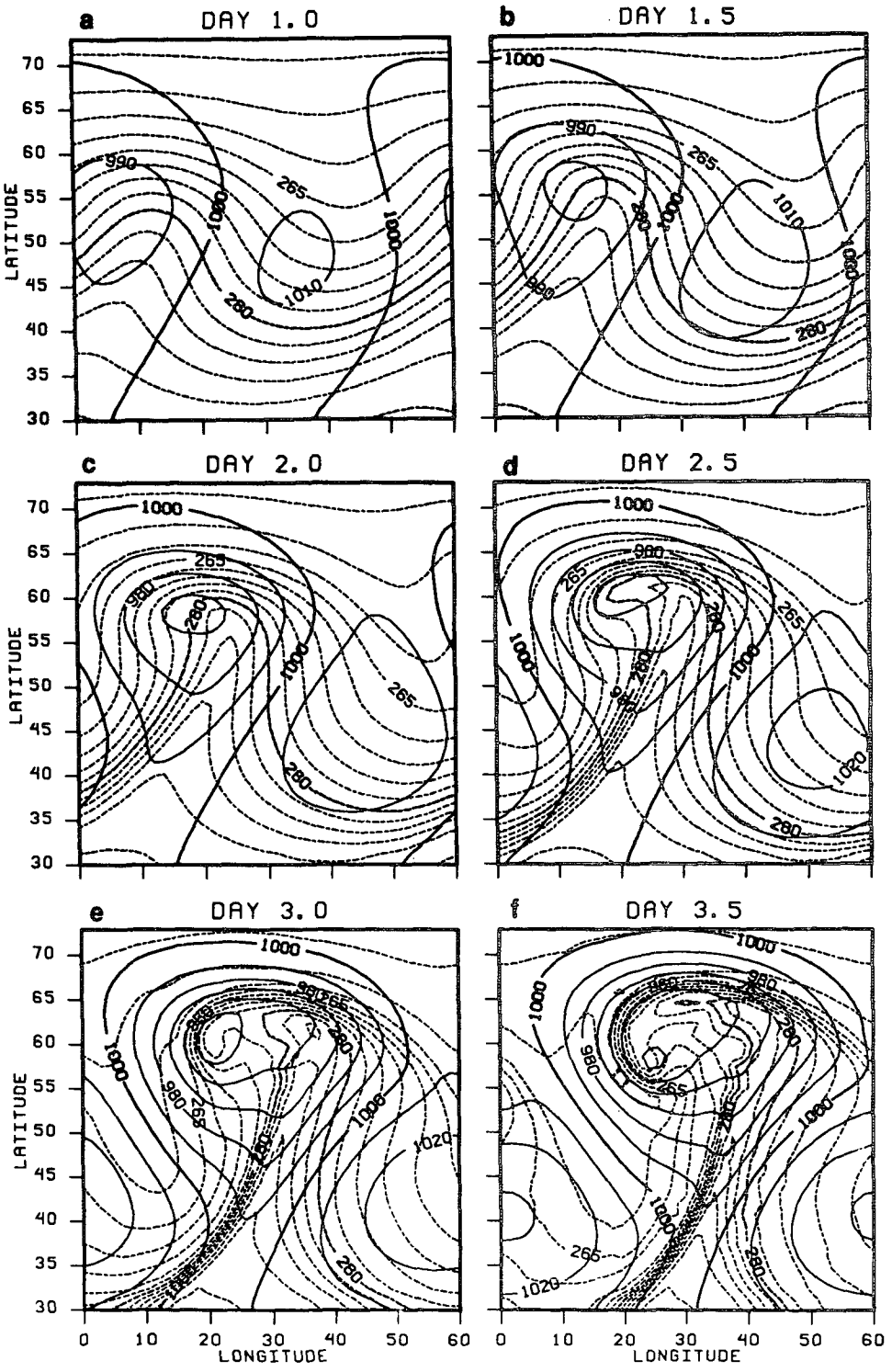

FIG. 4. As in Fig. 3 except for ocean drag.

no drag, ocean drag, and land drag, respectively. Only a broad baroclinic zone is initially present as in Eady's (1949) model. Strong cold fronts of similar intensity develop in all three cases, and propagate eastward slightly faster with decreasing surface drag. In no drag and ocean drag, warm fronts begin to form around day 2.0 east of the surface low. In the next 24 h, the westwardmost sections of these fronts start bending equa-

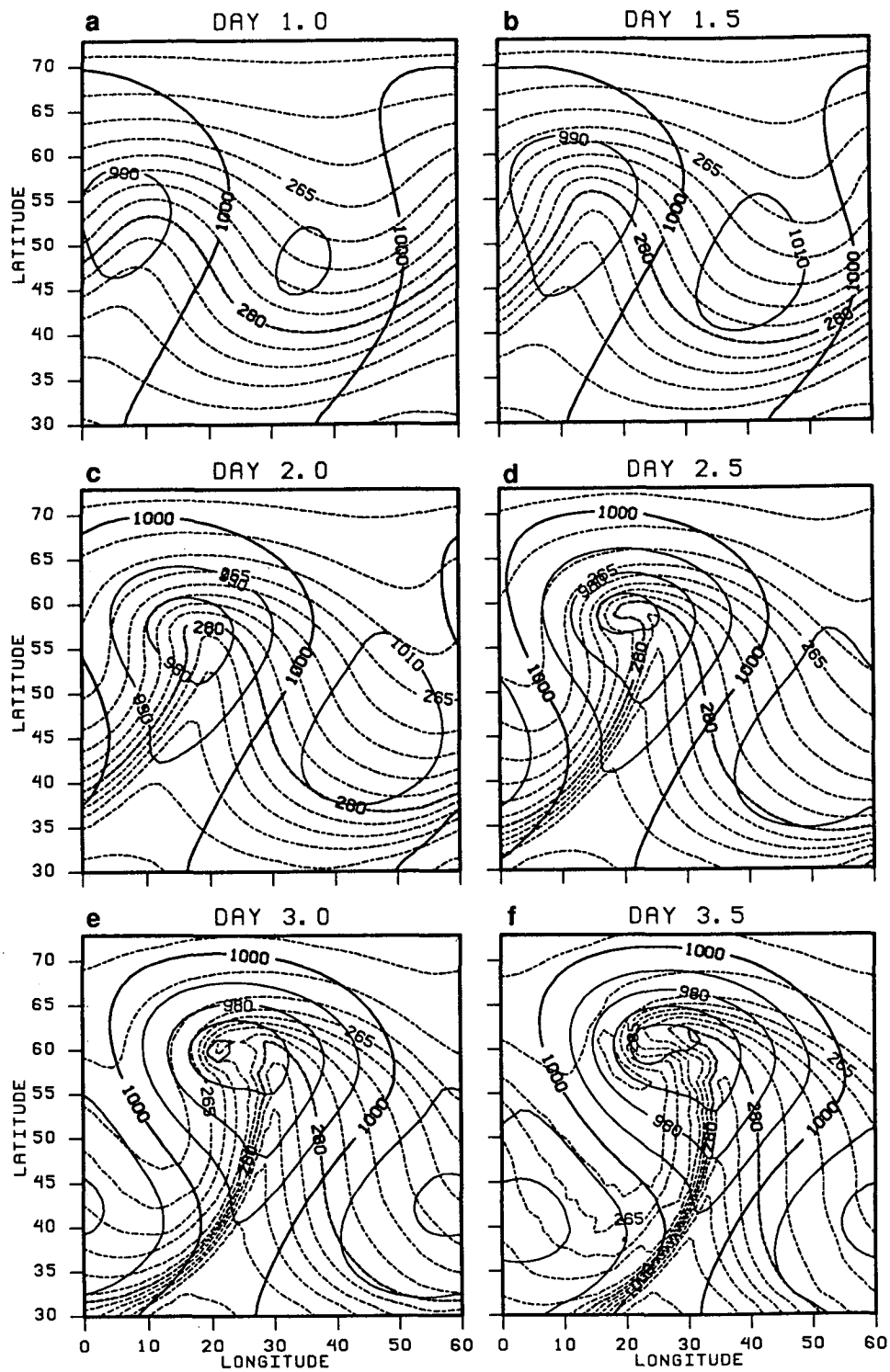

FIG. 5. As in Fig. 3 except for land drag.

torward. At day 3.0, maximum potential temperature gradients along the cold fronts are 8×10^{-5} K m^{-1} in no drag, and 7×10^{-5} K m^{-1} in ocean drag as well as in land drag. In no drag, the maximum temperature gradient at the poleward edge of the warm sector is 10×10^{-5} K m^{-1}, and that in the bent-back portion of the front is 8×10^{-5} K m^{-1}. In ocean drag, the corresponding temperature gradients are slightly weaker.

At day 3.5, the length of the warm-frontal zone is larger in no drag than in ocean drag, while a distinct warm-frontal zone does not develop in land drag. Nevertheless, there is an enhancement of the temperature gradient in a small area slightly northwest of the surface low in this simulation.

A comparison between the fields in Figs. 3, 4, and 5 indicates that surface friction weakens the development of the baroclinic wave. The surface lows deepen and move poleward up to day 2.5. During this time, the lows are at approximately the same latitude as the apexes of the 280-K isentropes in the warm sectors. The seclusions form later on, in no drag and ocean drag, and the surface lows move equatorward. The surface low in the former simulation becomes very deep (936 mb) at day 3, after a fall of about 27 mb in the previous 24 h. Drag-induced convergence reduces the deepening to 945 mb in ocean drag and 957 mb in land drag.

The surface low is farthest poleward at day 2.5 in no drag. The reduced poleward displacement of minimum surface pressure with increasing surface drag is consistent with weaker baroclinic waves and weaker meridional velocities. Consequently, isobars are tightly packed poleward of the surface low, in no drag and relatively weakly packed there in land drag.

An interesting feature of these simulations is the nonuniform decrease in wind speed as surface drag increases. Figure 6 shows that wind speeds are reduced in magnitude, especially near the warm front, with increasing surface drag. In no drag there is a low-level jet at day 3.0 of up to 44 m s^{-1} directed toward the developing warm front. The corresponding wind speed in ocean drag is 32 m s^{-1} and in land drag is 19 m s^{-1}. Within the warm fronts, winds are easterly to southeasterly at about 45 m s^{-1} in no drag, only slightly weaker in ocean drag, and southeasterly at about 18 m s^{-1} in land drag. Near the bent-back front, there are northerly winds of up to and exceeding 50 m s^{-1} in no drag. The wind-speed decrease with increasing surface drag near the warm front and poleward of the surface low is consistent with the variation in sea level pressure displayed in Figs. 3, 4, and 5. Behind the cold fronts, however, the wind speed is only slightly reduced with increasing surface drag.

The ageostrophic velocity gives insight into how the wind field near the warm fronts differs between simulations. Figure 7 shows the ageostrophic velocity of the lowest model level along with sea level pressure at day 2.0. Southeasterly ageostrophic flow of roughly 5 m s^{-1} from the surface high to the surface low is apparent in all three simulations. In no drag, the resulting acceleration produces a low-level jet in the warm sector. In land drag, the dynamic acceleration is largely balanced by frictional effects. The warm-sector winds, therefore, are relatively weak in this case. There is clearly flow toward low pressure in the cases with surface drag included (Figs. 7b and 7c).

Figure 8 presents vertical sections of potential temperature and horizontal velocity at day 3 along the dashed lines in Fig. 6 for no drag and land drag. The cross section in Fig. 8a passes through the cold- and bent-back frontal zones in no drag. Also displayed is the warm sector ahead of the cold front—where southwesterly winds increase in speed with height—the cold air behind the northeastern part of the cold front—where the winds are also southwesterly—and the warm seclusion—where the weak winds have an easterly component. The bent-back front extends into the midtroposphere but is most intense in the lower troposphere, where the northeasterly winds decay steadily with height. There is some similarity between Figs. 8a and 8b in features such as the warm pocket and the cold air behind the cold front. The cold front appears weak in Fig. 8b because the cross section is almost parallel to the front. The region of enhanced potential-

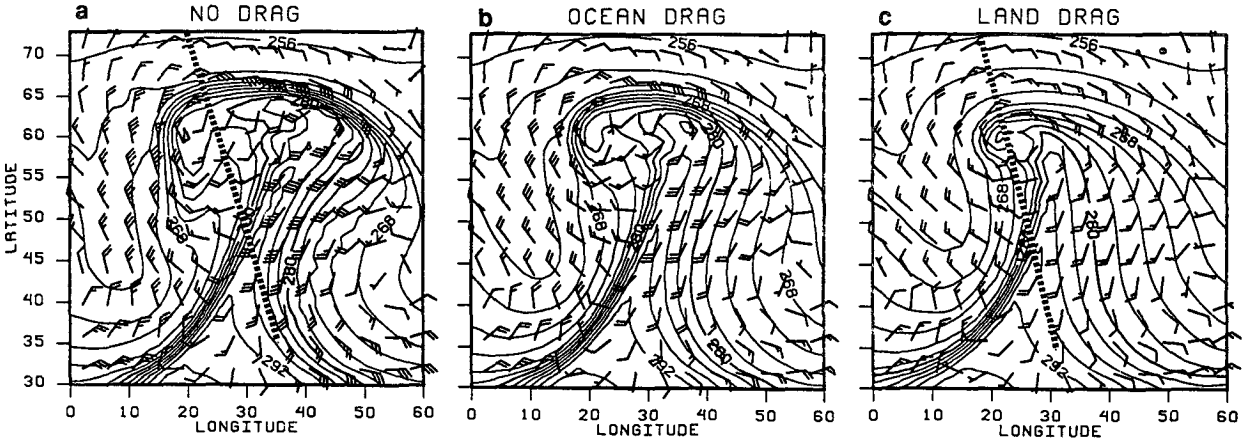

FIG. 6. Longitude–latitude plot at day 3 of the model's lowest level potential temperature (K, solid lines) and horizontal velocity (wind barbs) for (a) no drag, (b) ocean drag, and (c) land drag. The contour interval for potential temperature is 3 K; the thick, solid contour is 280 K. Flags, full wind barbs, and half-barbs indicate speeds of 50, 10, and 5 m s^{-1}, respectively.

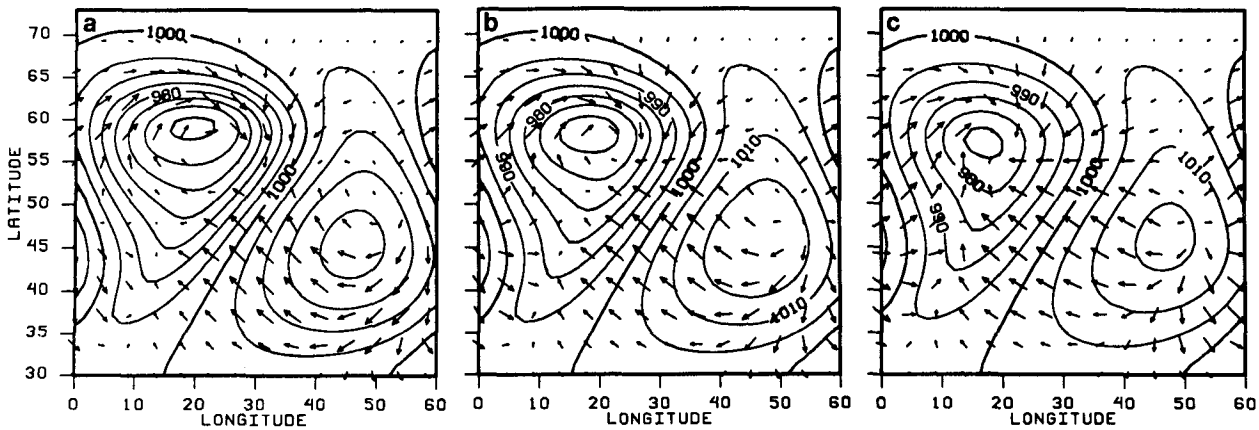

FIG. 7. Longitude–latitude contour plot at day 2 of ageostrophic velocity (arrows) for the model's lowest level and sea level pressure (mb, solid lines) in (a) no drag, (b) ocean drag, and, (c) land drag. The contour interval for sea level pressure is 5 mb.

temperature gradients poleward of the warm pocket in land drag, as seen in Fig. 5, is quite shallow. Wind speeds are generally weaker in Fig. 8b compared to those in Fig. 8a, especially poleward of the warm pocket.

At the cold front, all three simulations produce the characteristic large cyclonic turning in the isobars. At the warm front, there is also an abrupt cyclonic wind-direction shift in no drag and ocean drag and a more gradual change in wind direction in land drag. From Figs. 3 and 4, it is apparent that the cyclonic turning along the warm fronts increases with time in no drag and ocean drag. Figure 9 shows the absolute vorticity at day 2.0 for the three simulations. Maximum vorticities correspond to the cyclonic wind shifts along the frontal zones. Magnitudes of vorticity along the cold fronts are roughly similar in the simulations. Regions of large vorticity, in each case, are near the surface low and extend eastward along the warm front in no drag and to a lesser extent in ocean drag. The maximum

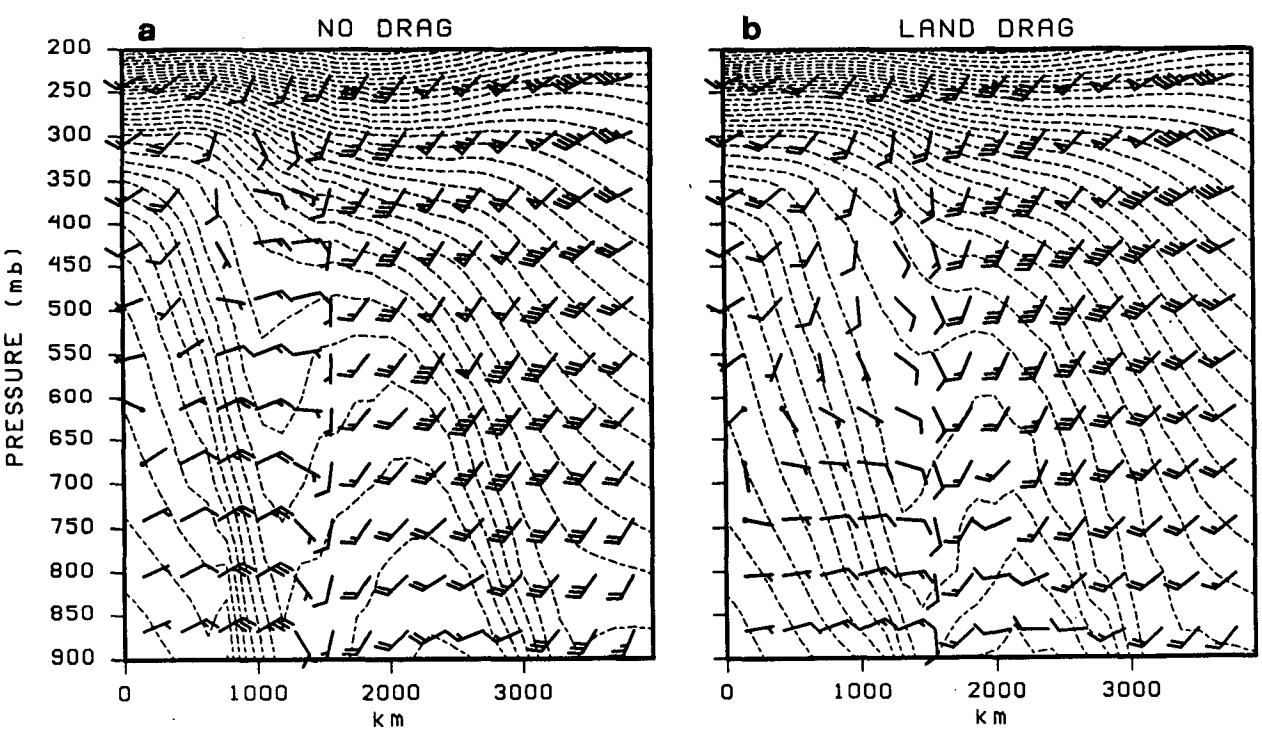

FIG. 8. Latitude–height plot at day 3 of potential temperature (K, solid lines) and horizontal velocity (wind barbs) in (a) no drag and (b) land drag. The contour interval for potential temperature is 3 K and 10 K above and below 350 K, respectively. Flags, full wind barbs, and half-barbs, respectively, indicate speeds of 50, 10, and 5 m s^{-1}.

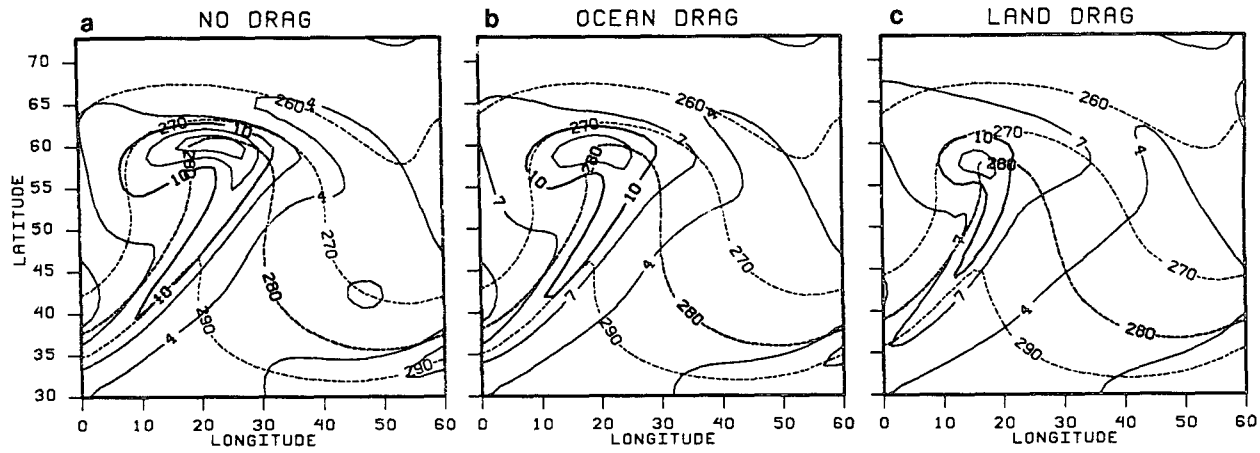

FIG. 9. Longitude–latitude contour plot at day 2 of absolute vorticity (10^{-5} s^{-1}, solid lines) and potential temperature (K, dashed lines) for the model's lowest level in (a) no drag, (b) ocean drag, and (c) land drag. The contour interval for vorticity is 3×10^{-5} s^{-1}; the thick solid contour is 10×10^{-5} s^{-1}. The contour interval for potential temperature is 10 K; the thick dashed contour is 280 K.

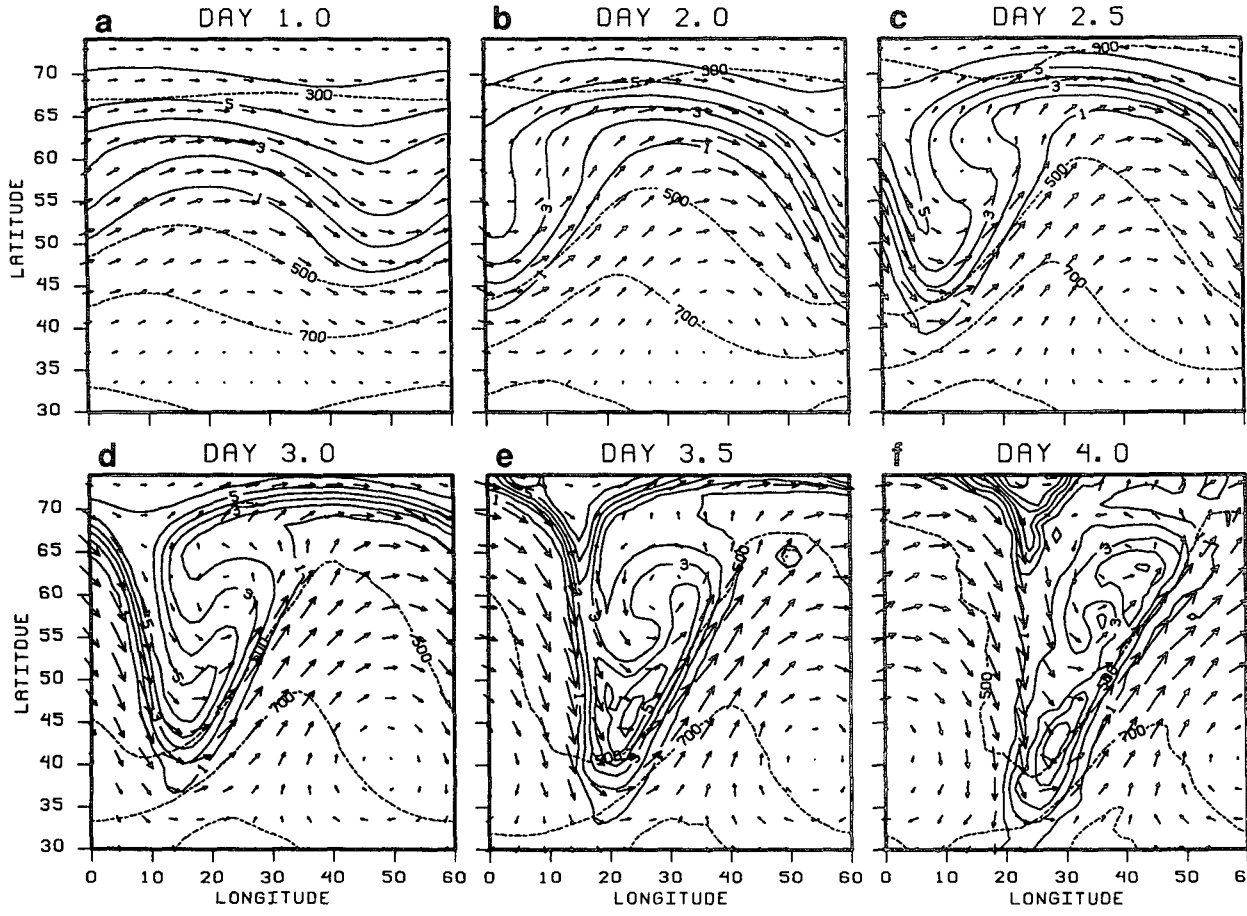

FIG. 10. Longitude–latitude plot of potential vorticity (PVU, solid lines), wind velocity (arrows), and pressure (mb, dashed lines) on the 300-K isentropic surface in no drag at (a) day 1.0, (b) day 2.0, (c) day 2.5, (d) day 3.0, (e) day 3.5, and (f) day 4.0. The contour interval for potential vorticity is 1 PVU. The contour interval for pressure is 200 mb.

values for these cases are 12.1×10^{-5} and 9.2×10^{-5} s^{-1}, respectively. It will be seen below that these cyclonic wind shifts are components in positive feedback processes leading to the intensification of the warm frontal zones.

We now focus on the evolution of the cyclone in no drag, including the formation of the warm-air seclusion, by using contour plots of Ertel's potential vorticity (PV) in potential vorticity units (PVU, Hoskins et al. 1985) on the surface $\theta = 300$ K, which goes from the upper troposphere at the pole to the lower troposphere in the subtropics (Fig. 10). As the cyclone intensifies, a tongue of high-PV air flows equatorward and another tongue of low-PV air flows polewards. The movement of the high- and low-PV tongues near the cyclone center corresponds well with that of regions of relatively cold and warm air, respectively, seen in Fig. 3. At day 3.0, the air behind the cold front is spreading out with the northern portion, associated with high-PV air at about 400 mb on the $\theta = 300$ K surface, moving northeastward and the southern portion moving southward. Notice that the cold front corresponds to large horizontal PV gradients. The wrap up of cold air associated with high PV and warm air associated with low PV continues to day 3.5 near the surface low. At this time, a pool of high-PV air near 40° latitude is essentially cutoff from its source region, and there is low-PV air in the seclusion. At day 4.0, the synoptic-scale wave is decaying due to barotropic processes, and the features of the seclusion have dissipated. The corresponding field for land drag is shown in Fig. 11. The weaker easterly and southerly flows (see Fig. 6) in this simulation inhibit the formation of a distinct seclusion.

The processes that intensify the frontal gradients of potential temperature are examined next. Following Miller (1948), we consider the equation for the rate of change in the magnitude of the horizontal potential-temperature gradient $|\nabla\theta|$,

$$\frac{d}{dt}|\nabla\theta| = \frac{\partial}{\partial t}|\nabla\theta| + \nabla|\nabla\theta|\cdot\mathbf{v} + \omega\frac{\partial}{\partial p}|\nabla\theta|$$

$$= \underbrace{-\frac{1}{2}(\nabla\cdot\mathbf{v})|\nabla\theta|}_{\text{(I-}\theta\text{)}} + \underbrace{\frac{1}{2}\cos(2\delta)D|\nabla\theta|}_{\text{(II-}\theta\text{)}}$$

$$\underbrace{-\frac{1}{|\nabla\theta|}\frac{\partial\theta}{\partial p}\nabla\omega\cdot\nabla\theta}_{\text{(III-}\theta\text{)}} + \underbrace{\frac{1}{|\nabla\theta|}\nabla\theta\cdot\nabla\frac{d\theta}{dt}}_{\text{(IV-}\theta\text{)}}, \quad (5)$$

where θ is potential temperature, ∇ is the horizontal gradient operator, $\mathbf{v}$ is horizontal velocity, ω is vertical velocity (dp/dt), and δ is the angle between $\nabla\theta$ and the axis of contraction for the fluid motion (or the angle between lines of constant potential temperature and the axis of dilatation). The quantity D is the deformation parameter for the horizontal component of the motion defined (in Cartesian coordinates) as

$$D = \left[\left(\frac{\partial u}{\partial x} - \frac{\partial v}{\partial y}\right)^2 + \left(\frac{\partial u}{\partial y} + \frac{\partial v}{\partial x}\right)^2\right]^{1/2}, \quad (6)$$

where u and v are the zonal and meridional wind components, respectively.

The changes in $|\nabla\theta|$ following a fluid parcel, which will be referred to as frontogenesis, are represented in the left-hand side of (5). Frontogenesis, therefore, is due to the combined effects of horizontal divergence and deformation (represented by I-θ and II-θ, respectively), tilting (represented by III-θ), and diabatic processes (represented by IV-θ). The corresponding signs imply that horizontal convergence and divergence are frontogenetical and frontolytical, respectively. Horizontal deformation may be frontogenetical or frontolytical depending on the orientation of the thermal field to the deformation field: namely, δ smaller or larger than $\pi/4$. Tilting is frontogenetical if the vertical circulation is thermally indirect ($\nabla\omega\cdot\nabla\theta > 0$).

Selected terms from (5) at 900 mb for day 2 in no drag are presented in Fig. 12. Frontogenesis is large and positive along the cold front and along the eastern section of the warm front (Fig. 12a), with the largest value in the warm front (11.8×10^{-10} K m^{-1} s^{-1}). Thus, the results of this simulation are in agreement with the findings of Mudrick (1974) that the warm frontogenesis is more intense and isolated from the cold frontogenesis in 3D adiabatic and inviscid simulations. Further, the frontogenesis values are of the same order of magnitude as in the simulations of Takayabu (1986) and Orlanski et al. (1985, dry case). Observed order of magnitudes of frontogenesis vary from 10^{-9} (Ogura and Portis 1982) to 10^{-7} K m^{-1} s^{-1} (Sanders 1955). In the region between the developing fronts, the frontogenesis is small, yet positive. Thus, in no drag, the development of separated warm and cold fronts is due to a gap between regions of intense warm and cold frontogenesis.

The contribution of horizontal deformation at day 2 is largely responsible for the frontogenesis at 900 mb, as shown by the close resemblance between Figs. 12a and 12c. This contribution is roughly five times and three times that of divergence along the cold and warm fronts, respectively (see Fig. 13a). Mudrick (1974) and Orlanski et al. (1985) obtain roughly similar results in their dry simulations. Ogura and Portis (1982) find a relatively higher contribution of divergence (roughly 70% that of deformation) for a cold front in their observational study. Horizontal advection (Fig. 12d) tends to provide the largest contribution to the Eulerian rate of change of $|\nabla\theta|$ around both frontal zones (Fig. 12b). It is apparent that the local increase in $|\nabla\theta|$ in the western section of the warm front is due to horizontal advection by the strong easterly winds.

Figure 14 presents terms of (5) at day 2.5 in no drag. A comparison with Fig. 12 shows that the magnitude of all these terms has increased substantially in the last 12 h. Horizontal advection to the west of the surface

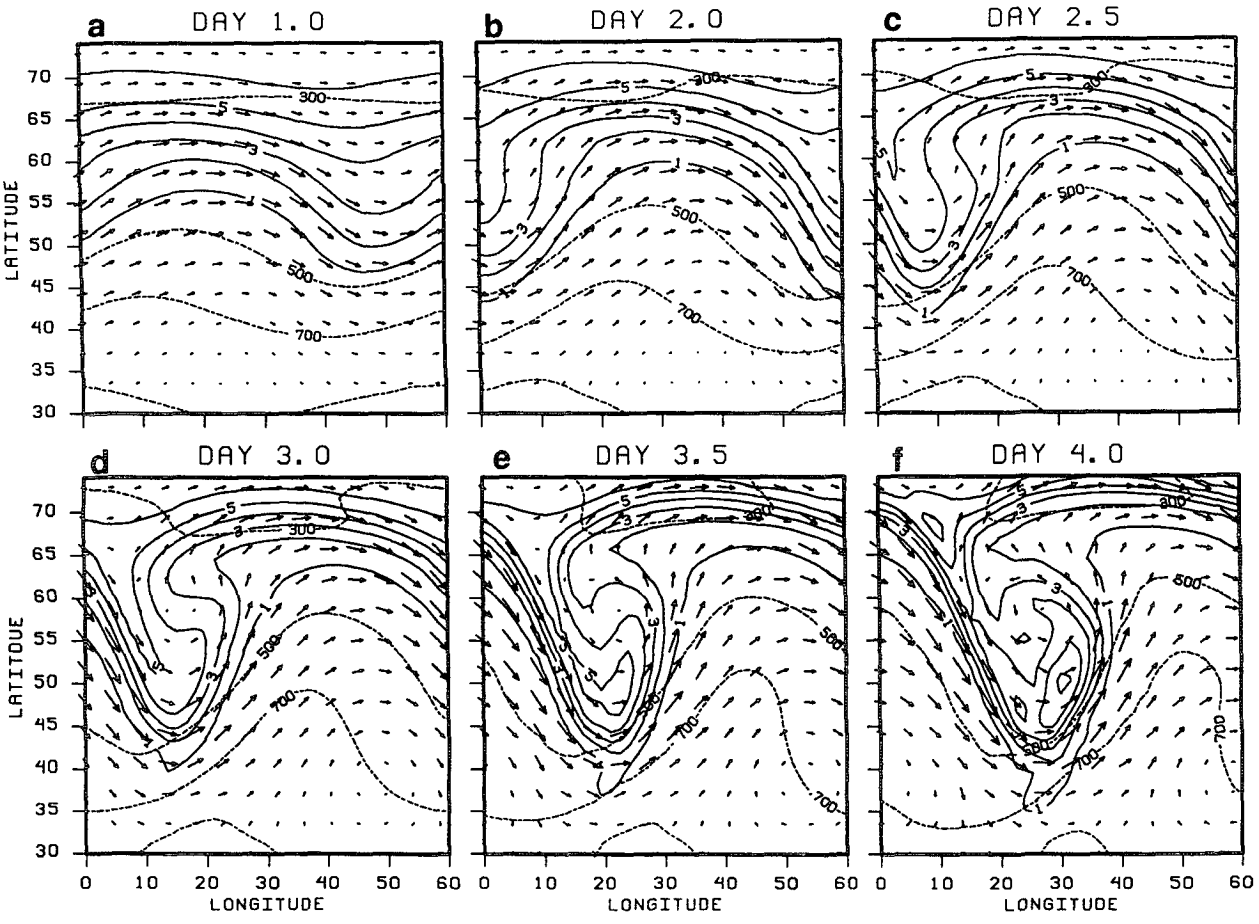

FIG. 11. As in Fig. 10 except for land drag.

low is now bending the western edge of the front south. The tendency of advection to form a bent-back front is weakly opposed by frontolysis in the strong northeasterly and northerly winds, which exceed 35 m s^{-1} at this time. Qualitatively similar results (not shown) are obtained in ocean drag, although frontogenesis is generally weaker along the warm front. Takayabu (1986) also finds that the bent-back front in his inviscid integration results from horizontal advection.

To compare the frontogenesis in no drag with that in land drag, a similar analysis is carried out for the latter simulation (see Fig. 15). At day 2.0, the frontogenesis in the cold-frontal zone is larger in land drag than in no drag (6.6×10^{-10} and 4.3×10^{-10} K m^{-1} s^{-1}, respectively, at 45° latitude). This is primarily due to the increase with surface drag of the contribution of divergence since that of deformation is almost constant with surface drag (4.6×10^{-10} K m^{-1} s^{-1} in no drag and 4.5×10^{-10} K m^{-1} s^{-1} in land drag at 45°). The frontogenesis on the poleward edge of the warm sector, on the other hand, is much smaller than in no drag. This is primarily due to the decrease with surface drag of the contribution of deformation, although that of divergence is also smaller than in no drag. The locally enhanced temperature gradient slightly northwest of the surface low in land drag is largely due to surface convergence. In further contrast to no drag, the contribution of advection to the local change is also very small in land drag due to the weakness of the easterly wind speed and temperature gradient in this region. Our results are in agreement with the finding by Mudrick (1974) that the contribution of divergence, although smaller than that of deformation, is important for the differing rates of warm and cold frontogenesis. The varying contributions of divergence and deformation to the frontogenesis in our simulations are summarized in Table 1.

It follows that we can simulate some of the features of the Shapiro and Keyser (1990) model of ocean cyclogenesis with an adiabatic or quasi-adiabatic model. Bent-back fronts develop in the simulations with relatively small surface drag due to large horizontal advections. The break between the simulated cold and warm fronts is due to a gap between regions of strong cold and warm frontogenesis. Horizontal deformation is largely responsible for both warm and cold fronto-

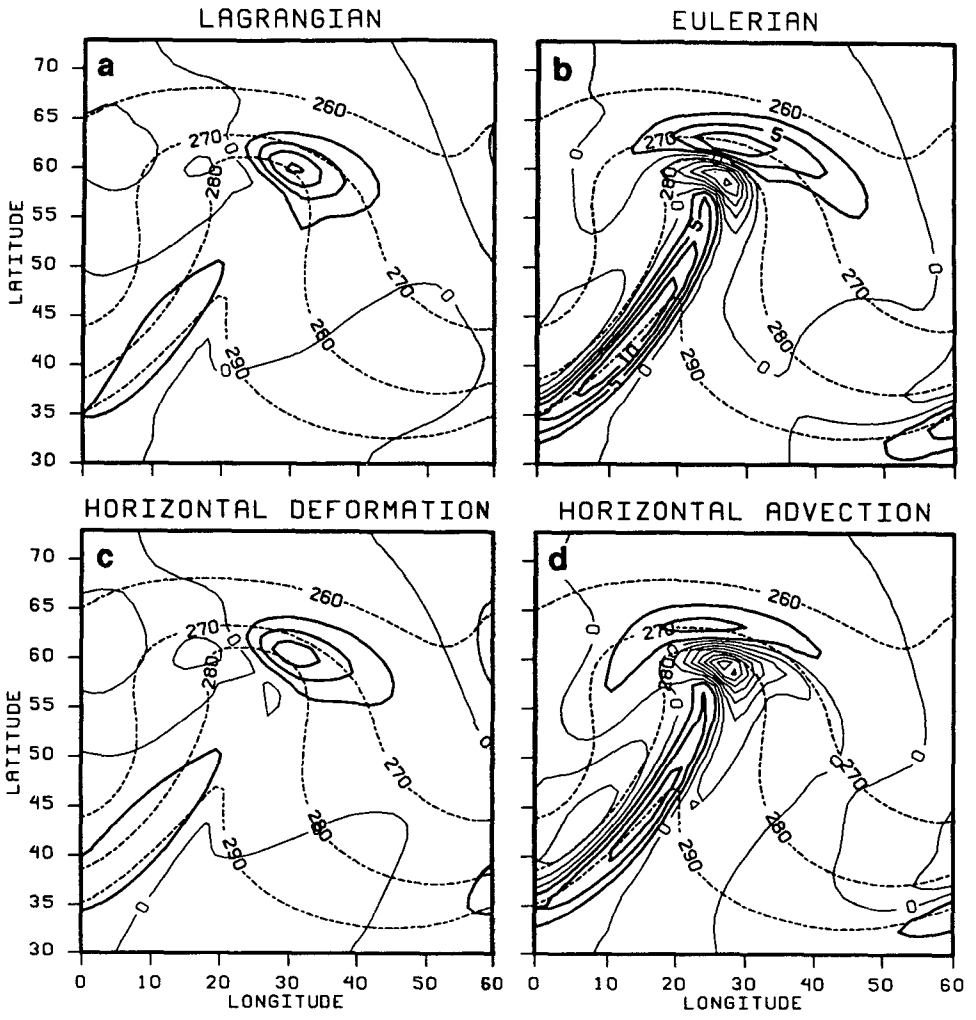

FIG. 12. Longitude–latitude contour plot at day 2 of terms in (5) (10^{-10} K m^{-1} s^{-1}, solid lines) and potential temperature (K, dashed lines) at 900 mb in no drag. The contour interval for frontogenesis terms is 2.5×10^{-10} K m^{-1} s^{-1}. Thick, solid contours indicate positive values. The contour interval for potential temperature is 10 K. (a) Lagrangian rate of change, (b) Eulerian rate of change, (c) contribution of horizontal deformation, and (d) contribution of horizontal advection.

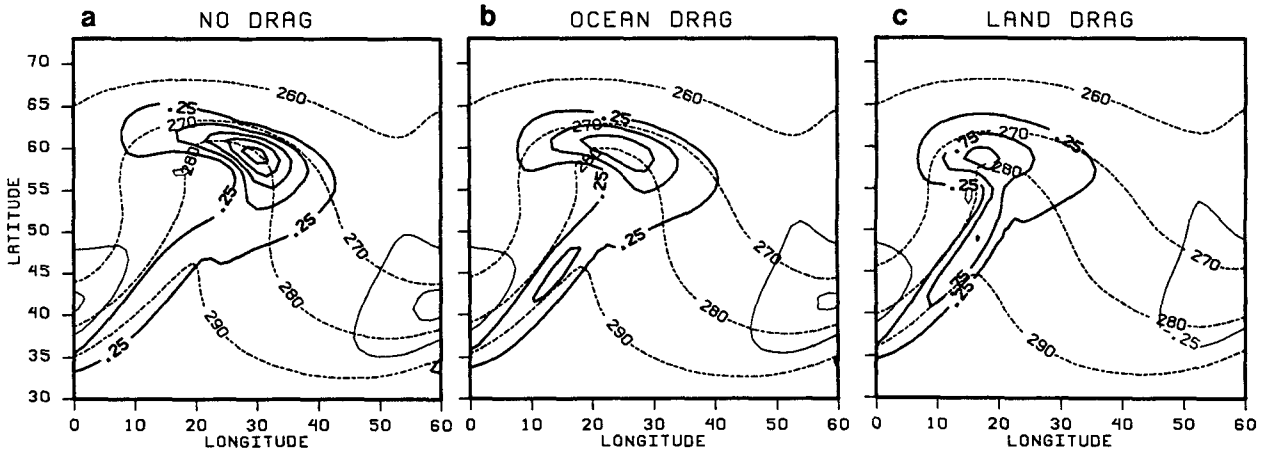

FIG. 13. As in Fig. 9 except for the contribution of divergence to frontogenesis (10^{-10} K m^{-1} s^{-1}, solid lines) at 900 mb. The contour interval for frontogenesis is 0.5×10^{-10} K m^{-1} s^{-1}. Thick, solid lines indicate positive values.

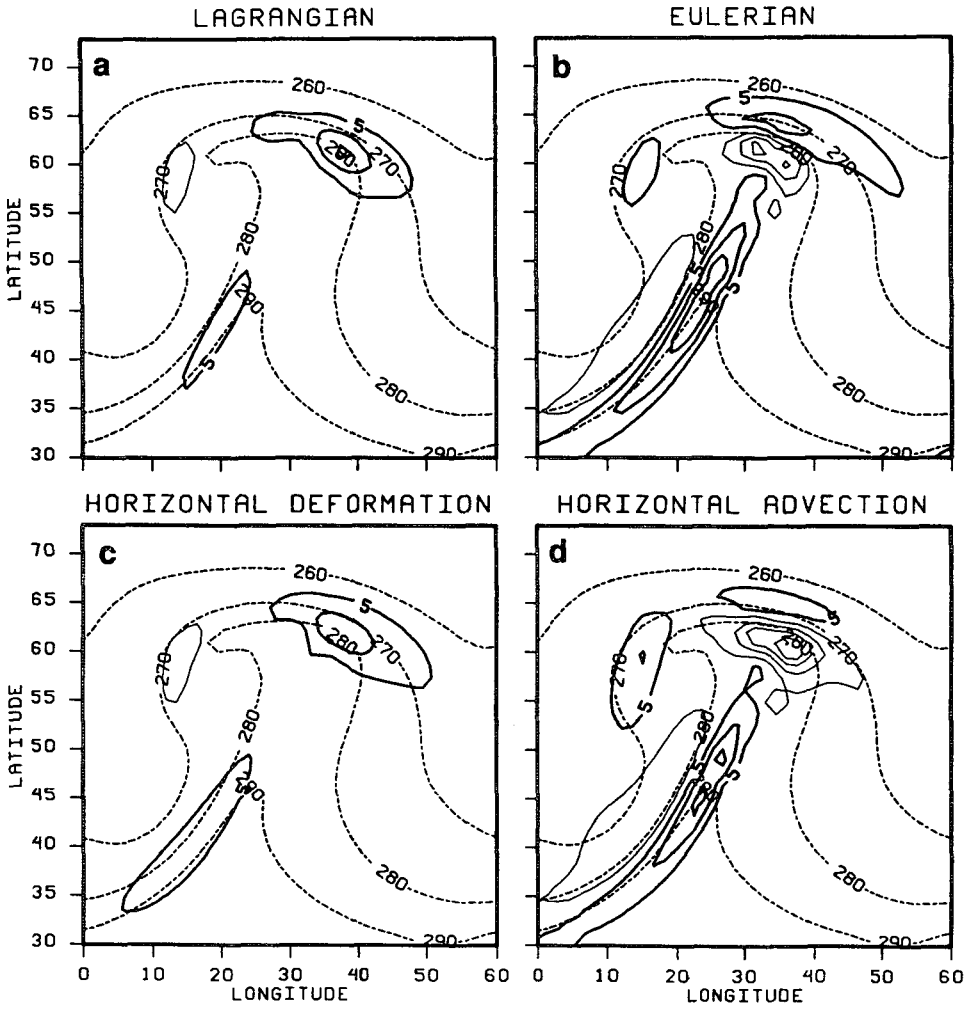

FIG. 14. As in Fig. 12 except for day 2.5. The contour interval for frontogenesis terms is 10×10^{-10} K m^{-1} s^{-1}.

genesis. The role of horizontal divergence varies between cold and warm frontogenesis and with surface drag. Surface drag reduces the low-level wind speed considerably near the warm front and to a lesser extent near the cold front. Also, the intensity of simulated warm fronts is found to be very sensitive to surface drag, while that of simulated cold fronts is relatively insensitive to surface drag.

5. Feedbacks in simulated frontogenesis

Figure 16 shows the horizontal divergence for the model's lowest level at day 2.0 in no drag, ocean drag, and land drag. The surface convergence at the cold front is considerably larger in land drag than in no drag. The zones of convergence along and ahead of, and divergence behind, the cold fronts, are integral parts of thermally direct circulations associated with these fronts. Figure 17 displays the vertical velocity field at day 2 for 700 mb, which shows rising along and sinking behind the cold fronts. The ascent is typically 100–150 mb day^{-1} with values in land drag slightly larger than those in the other simulations. Maxima of subsidence are 358 mb day^{-1} in no drag, 339 mb day^{-1} in ocean drag, and 313 mb day^{-1} in land drag.

At the poleward edge of the warm sector, rising motion is highly sensitive to the values of the drag coefficient as locations of the maxima change and magnitudes decrease as surface friction increases. Maximum ascent is farthest east and largest in no drag, and nearest the surface low in land drag. The maxima of ascent at day 2.0 are 347 mb day^{-1} in no drag, 250 mb day^{-1} in ocean drag, and 259 mb day^{-1} in land drag. Regions of largest ascent in Fig. 17 correspond to regions of largest vorticity in Fig. 9 and to regions of strongest surface convergence in Fig. 16. Therefore, the development of the cyclonic wind shifts along the

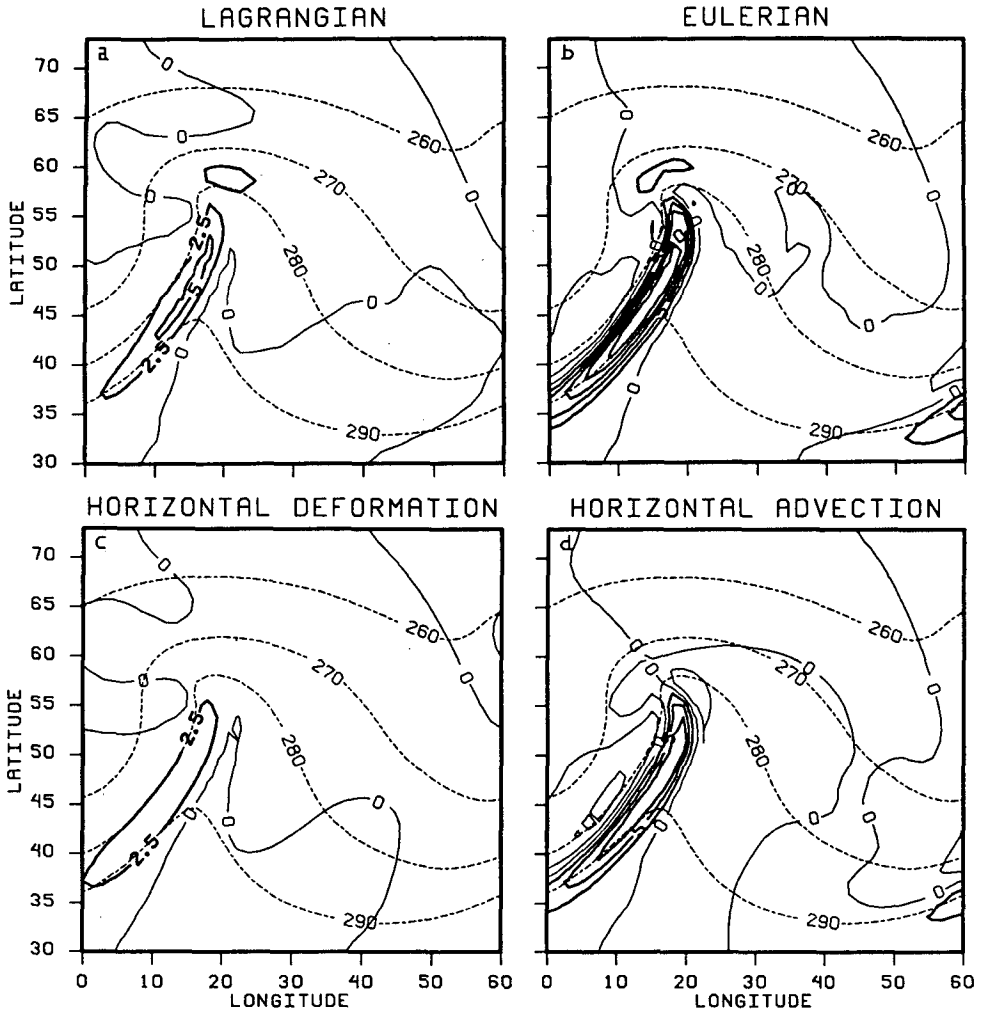

FIG. 15. As in Fig. 12 except for land drag.

cold fronts in all three simulations as well as along the warm fronts in no drag and ocean drag, is associated with the local maxima in cyclonic vorticity, frontogenetical deformation and convergence, and, apparently, the vertical circulations near the frontal zones.

The time evolution of the deformation term $D\cos(2\delta)$ in (5) during the early stages of frontogenesis in no drag is shown in Fig. 18. Over this period, the doubling time of deformation, vorticity, and convergence (not shown) along the eastern section of the developing warm front is about 12 h, which is significantly faster than that of low-level wind speed. This suggests that the warm frontogenesis is enhanced by positive feedback. The doubling time for the magnitude of deformation is slightly longer along the cold front. Faster growth of convergence and vorticity along the warm-advection front than the cold-advection front is also found in 2D simulations performed by Keyser and Pecnick (1987).

TABLE 1. Effects of surface drag.

Cold front	Warm front
Deformation, the dominant frontgenetical process, is relatively independent of surface drag	*Deformation,* the dominant frontogenetical process, strongly decreases with increasing surface drag
Divergence, which is small, *increases* with increasing surface drag	*Divergence,* which is also relatively small, *decreases* with increasing surface drag

The effect of surface drag on the feedbacks along the warm and cold fronts is next examined. Figure 19 presents the evolution of $D\cos(2\delta)$ in land drag. Compared to no drag, deformation increases at approximately the same rate along the cold front and at less than half the rate northeast of the warm sector. This suggests that the feedback process that enhances warm frontogenesis is inhibited by surface drag, while that

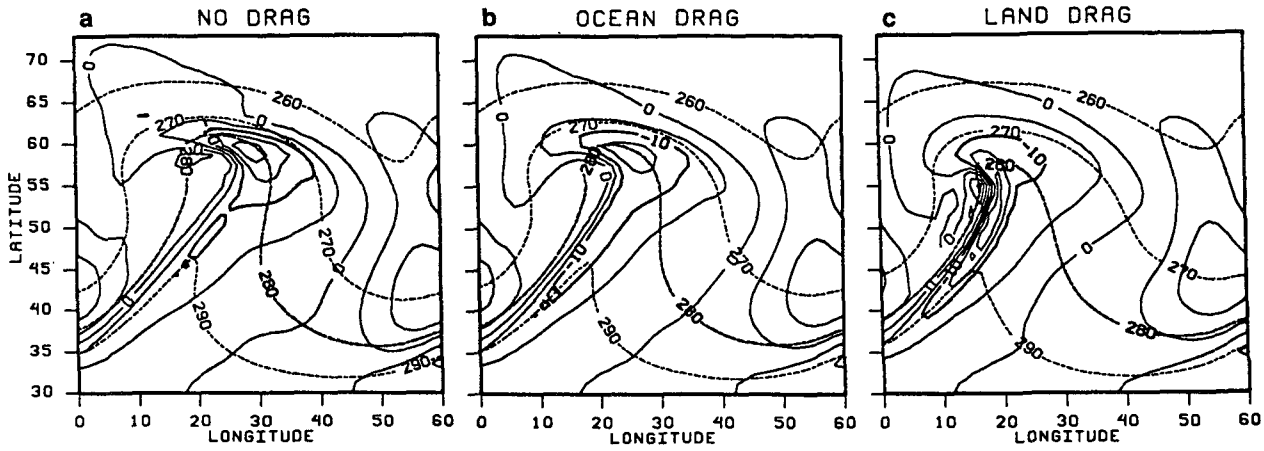

FIG. 16. As in Fig. 9 except for horizontal divergence (10^{-6} s^{-1}, solid lines). The contour interval for divergence is 5×10^{-6} s^{-1}; the thick, solid contour is -10×10^{-6} s^{-1}.

of cold frontogenesis is relatively insensitive to surface drag.

To gain insight into the mechanisms that are involved in the feedback process and are affected by friction, the development of the associated vertical circulations is evaluated. This is appropriate as horizontal convergence increases the vorticity along the frontal zones. Horizontal convergence also increases the deformation along the frontal zones. This is demonstrated by the equations for the time rate of change of deformation terms, D_1 and D_2, in Cartesian coordinates under frictionless and adiabatic conditions,

$$\frac{d}{dt} D_1 = \frac{d}{dt}\left(\frac{\partial u}{\partial x} - \frac{\partial v}{\partial y}\right) = -(\nabla \cdot \mathbf{v}) D_1 + f(D_2)_{ag} - \frac{\partial \omega}{\partial x}\frac{\partial u}{\partial p} + \frac{\partial \omega}{\partial y}\frac{\partial v}{\partial p} + \beta u_{ag}, \quad (7)$$

$$\frac{d}{dt} D_2 = \frac{d}{dt}\left(\frac{\partial u}{\partial y} + \frac{\partial v}{\partial x}\right) = -(\nabla \cdot \mathbf{v}) D_2 - f(D_1)_{ag} - \frac{\partial \omega}{\partial y}\frac{\partial u}{\partial p} - \frac{\partial \omega}{\partial x}\frac{\partial v}{\partial p} + \beta v_{ag}, \quad (8)$$

$$D = (D_1^2 + D_2^2)^{1/2}, \quad (9)$$

where f is the Coriolis parameter, and β is df/dy. From the first terms on the right-hand side (rhs) of both (7) and (8), it is seen that frontal convergence can increase the magnitude of horizontal deformation with time. Consistently, the wind shifts along frontal zones, which can be quantitatively measured in terms of vorticity and deformation, are observed to intensify with time in Figs. 3–5.

To gain insight into the development of frontal convergence, the vertical motions are examined. Keyser and Pecnick (1987) use diagnostic equations for the

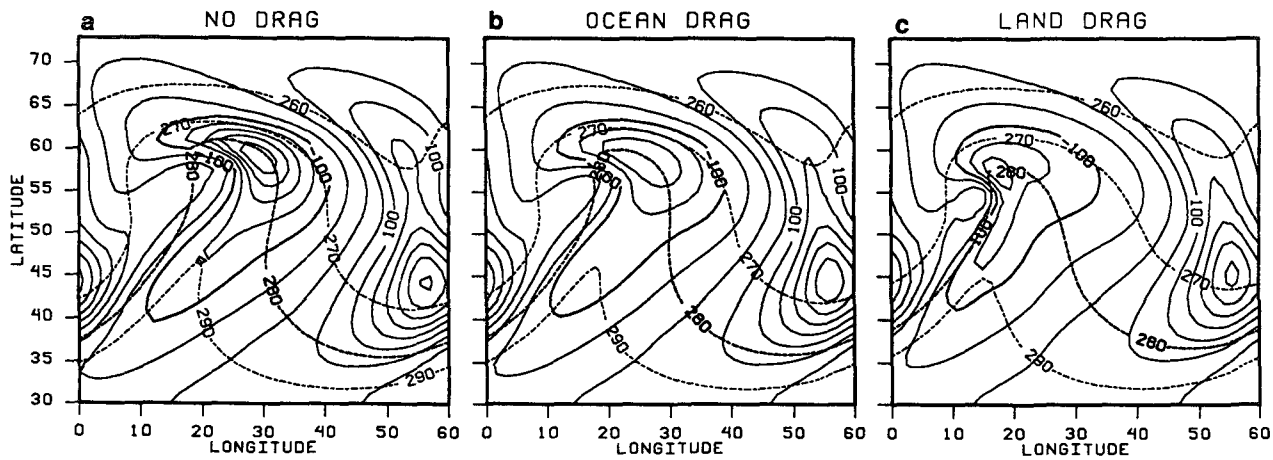

FIG. 17. As in Fig. 9 except for the vertical velocity at 700 mb (mb day^{-1}, solid lines) and the potential temperature for the model's lowest level (K, dashed lines). The contour interval for vertical velocity is 50 mb day^{-1}; the thick, solid contour is -100 mb day^{-1}.

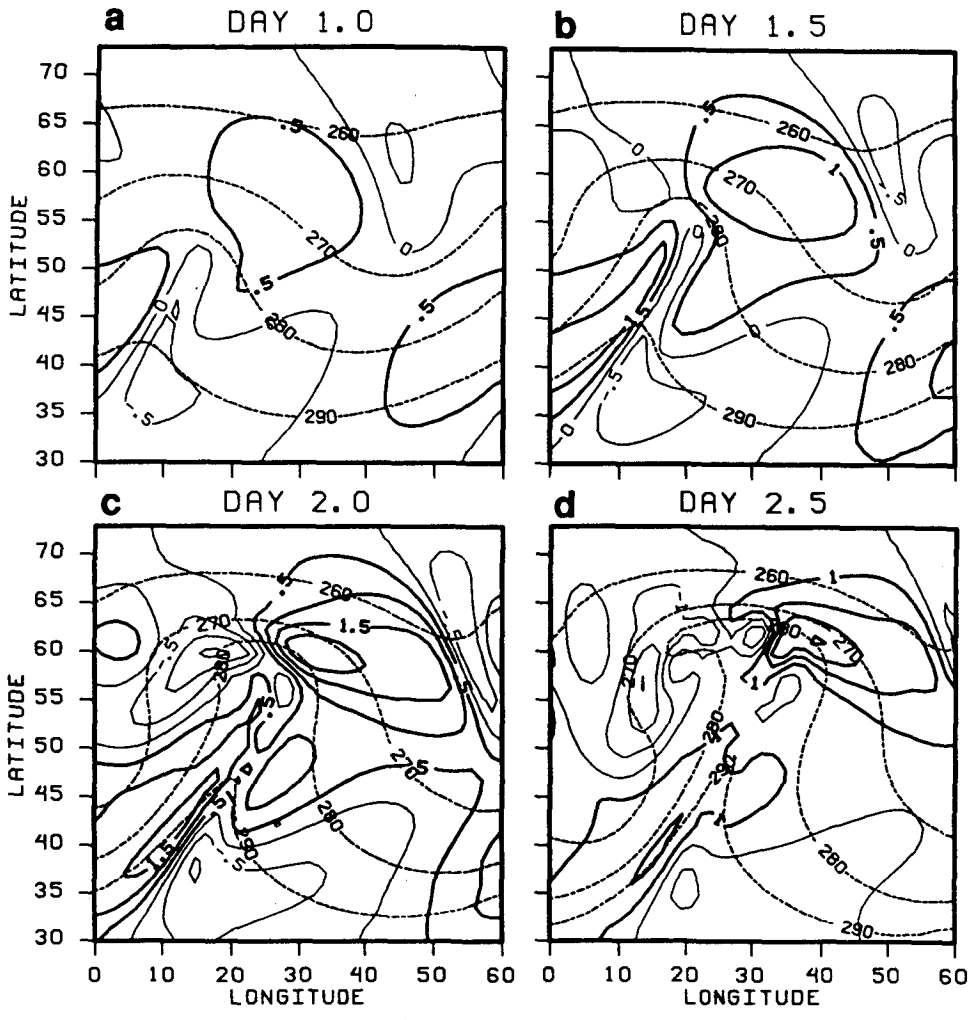

FIG. 18. Longitude–latitude contour plot of $D\cos(2\delta)$ (10^{-5} s^{-1}, solid lines) and potential temperature (K, dashed lines) for 900 mb in no drag at (a) day 1.0, (b) day 1.5, (c) day 2.0, and (d) day 2.5. The contour interval for $D\cos(2\delta)$ is 0.5×10^{-5} s^{-1} for (a), (b), and (c) and 1.0×10^{-5} s^{-1} for (d). Thick, solid contours indicate positive values. The contour interval for potential temperature is 10 K.

vertical velocity to examine frontogenetical feedbacks in their simulations. Following a similar approach, we consider the quasigeostrophic omega equation,

$$-\frac{R}{f_0 p}\left(\frac{p}{p_0}\right)^{\kappa}\frac{\partial\overline{\theta}}{\partial p}\nabla^2\omega + f_0\frac{\partial^2}{\partial p^2}\omega = \frac{\partial}{\partial p}[\nabla(\zeta_g + f)\cdot\mathbf{v}_g] + \frac{R}{f_0 p}\left(\frac{p}{p_0}\right)^{\kappa}\nabla^2(\nabla\theta\cdot\mathbf{v}_g), \quad (10)$$

where f_0 is a 10^{-4} s^{-1}, R is the gas constant, κ is $2/7$, p_0 is 1000 mb, ζ is vorticity, the subscript g implies geostrophic quantities, and $\partial\overline{\theta}/\partial p$ is function of pressure only. The usual method of qualitative analysis (e.g., Hoskins 1990) associates rising (sinking) motions with positive (negative) values on the rhs (the "forcing") of (10). By this method, we also expect a positive forcing contribution from the thermal forcing, the second term on the rhs in locations where warm advection is a maximum (i.e., near warm fronts).

Figure 20 displays the forcing at day 2.0 in no drag, ocean drag, and land drag at 800 mb obtained using ζ and $\mathbf{v}$ instead of ζ_g and $\mathbf{v}_g$, respectively, in (10). This substitution is reasonable when (10) is valid. The vectors displayed are horizontal $\mathbf{Q}$ vectors taken here as

$$\mathbf{Q} = -\nabla\mathbf{v}\cdot\nabla\theta. \quad (11)$$

The horizontal locations of maxima in net forcing [the rhs of Eq. (10)] in Fig. 20 are well correlated with locations of maxima in ascent in Fig. 17. Net forcing has roughly similar values along the cold fronts in all three simulations. Along the warm fronts, however, net forcing decreases substantially with increasing surface drag. The largest values are 22.6×10^{-14} s^{-2} Pa^{-1} in no drag and 7.0×10^{-14} s^{-2} Pa^{-1} in land drag. Vor-

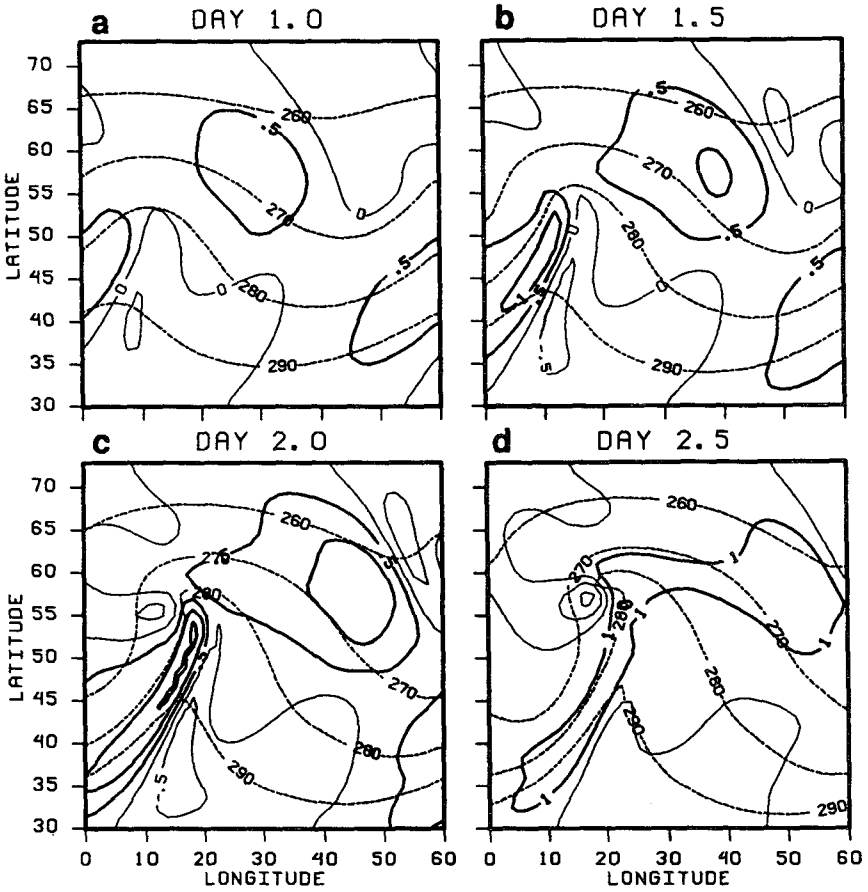

FIG. 19. As in Fig. 18 except for land drag.

ticity forcing and thermal forcing both contribute to the maximum in net forcing in no drag. The vorticity-forcing maximum is equatorward of the 280-K isentrope in Fig. 20a. Cancellation between the terms on the rhs of (10) is seen there (Hoskins et al. 1978; Trenberth 1978). The thermal-forcing term dominates poleward of the 280-K isentrope in no drag. The decrease in net forcing along the warm front with increasing surface drag appears to be largely associated with the accompaning decrease in thermal forcing. Maximum thermal forcing is 19.5×10^{-14} s^{-2} Pa^{-1} in no drag and 7.2×10^{-14} s^{-2} Pa^{-1} in land drag. This is related to the decrease in maximum, instantaneous potential temperature advection from 43.6 K day^{-1} in no drag to 22.1 K day^{-1} in land drag at 800 mb for day 2. Thus, analysis based on quasigeostrophic theory can help us understand the differring sensitivities of warm and cold fronts to surface drag.

These results suggest the following explanation of the impact of surface drag on frontogenesis. As surface drag increases, the surface low pressure system is weakened by Ekman pumping, and the surface wind speed is reduced, especially in the warm sector. This in itself weakens the frontogenesis. The effects are exacerbated by feedback as the reduced warm-air advection is associated with reduced ascent and low-level convergence. The frontal convergence has an important role in the positive feedback process, as it can intensify the deformation and vorticity at the warm front. Consequently, surface drag plays a frontolytical role in warm frontogenesis. With relatively low values of surface drag, as in the ocean-drag simulation, the warm front is slightly weaker than would be the case without drag. With higher values, as in the land-drag simulation, the feedback is hindered sufficiently to prevent a distinct warm front from forming.

The intensity of simulated cold fronts, on the other hand, is not very sensitive to surface drag. Postfrontal wind speeds are only slightly reduced by surface drag behind the cold front. Furthermore, the results of the simulations show that the quasigeostrophic forcing of vertical motion is much less sensitive to surface drag along cold fronts than along warm fronts. The thermal forcing term in (10) can also be used to explain the varying sensitivity to surface drag, as it suggests that a decrease in the maximum warm advection will result in weaker ascent near warm fronts. Near cold fronts, however, a decrease in thermal advection does not im-

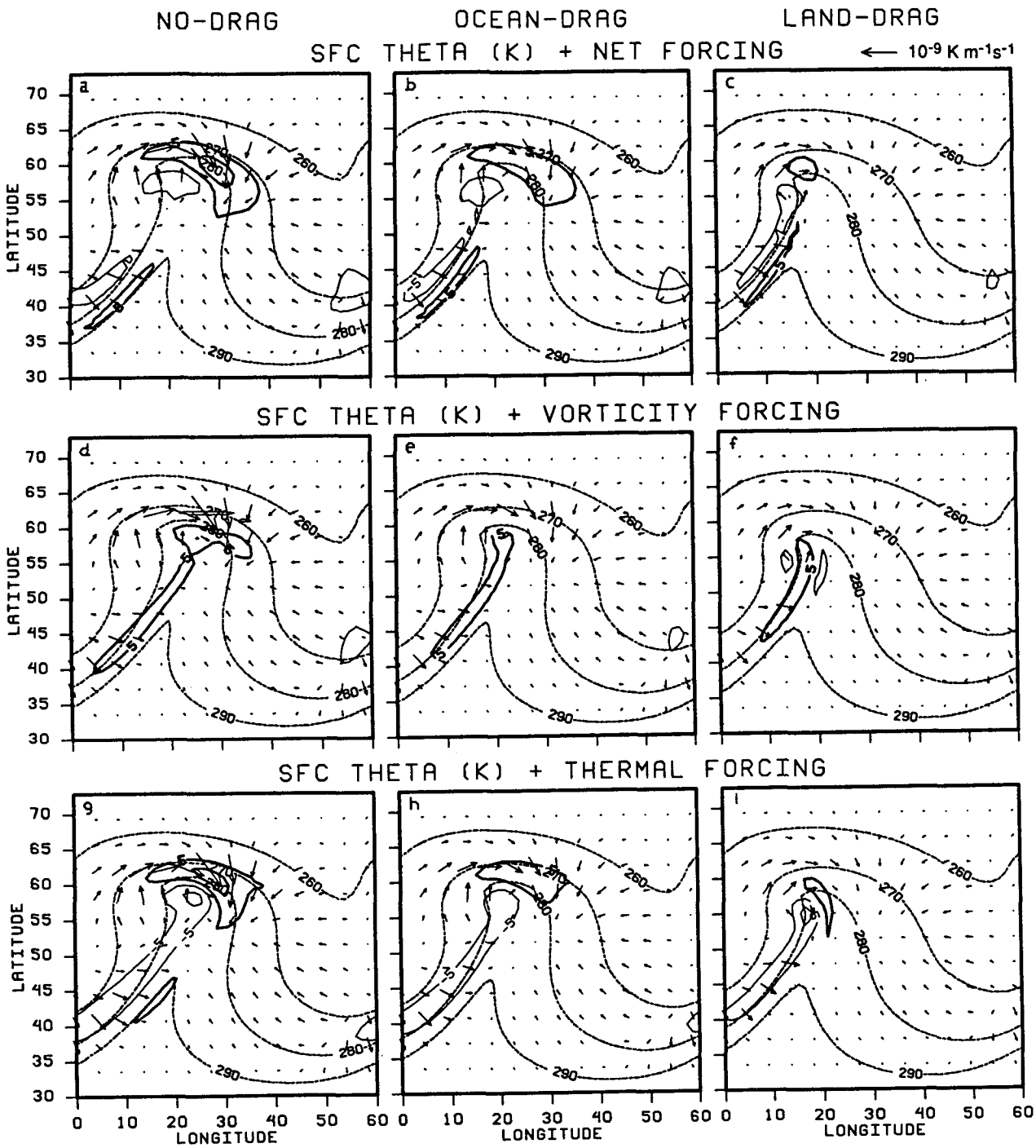

FIG. 20. Longitude–latitude contour plot at day 2 of the vertical-velocity forcing (10^{-14} s^{-2} Pa^{-1}, solid lines) and Q vectors (K m^{-1} s^{-1}, arrows) for 800 mb, and model's lowest-level potential temperature (K, dashed lines) (a) net forcing in no drag, (b) net forcing in ocean drag, (c) net forcing in land drag, (d) vorticity forcing in no drag, (e) vorticity forcing in ocean drag, (f) vorticity forcing in land drag, (g) thermal forcing in no drag, (h) thermal forcing in ocean drag, and (i) thermal forcing in land drag. Contour intervals are 10×10^{-14} s^{-2} Pa^{-1} for forcing and 10 K for potential temperature. Thick, solid lines indicate positive forcings.

ply weaker ascent from the thermal forcing. Thus, although cold fronts in our simulations intensify slower than the warm front in no drag, the intensity of the "cold advection" process appears to be less sensitive to surface drag. Furthermore, Hoskins (1990) shows that surface friction-induced inflow toward lower pres-

sure implies increasing surface convergence with increasing surface relative vorticity. Accordingly, the cyclonic wind shift at the cold front in land drag is associated with larger surface convergence than in no drag.

In summary, warm frontogenesis is enhanced by positive feedback involving warm advection, deformation, vorticity, and the vertical circulation when surface drag is small. When surface drag is large, the wind speed and the corresponding warm advection and "forcing" of ascent are reduced. Correspondingly, frontogenetical convergence, vorticity, and deformation grow at a slower rate. Along the cold front, however, forcing of vertical motion, and accordingly frontogenesis, are not very sensitive to surface drag.

6. Connection of surface fronts to the upper-tropospheric wave

Here, the interaction of the flow in the upper troposphere with that at lower levels is examined. Previously, it was shown that surface drag weakens thermal advection in the lower and middle troposphere. This is consistent with weaker synoptic waves resulting from increased surface drag. The influence of variable surface drag on the largest magnitudes of flow variables at 300 mb for day 2.0 is shown in Table 2. The synoptic wave in the upper troposphere is weakened by surface friction as the 300-mb maxima of geopotential height variations and wind speed are reduced by about 20% and 10%, respectively, in land drag from the corresponding maxima in no drag.

We now examine components of vertical circulation in the upper troposphere and relate them to components in the lower troposphere. It is apparent from Fig. 17 and Table 2 that an increase in surface drag results in weaker vertical circulations near the warm front and smaller ageostrophic wind speeds at 300 mb. In the upper troposphere, the percent decrease in ageostrophic wind speed with increasing surface friction is much larger near the ridge than near the trough. The horizontal divergence associated with the ageostrophic flow at 300 mb is, therefore, most sensitive to surface drag near the ridge, that is, above the warm front. Further, both the upper-tropospheric divergence above the cold front and the surface convergence along the cold front increase with increasing surface drag. Thus, the sensitivity of the lower-tropospheric flow to surface drag is consistent with the sensitivity of the upper-tropospheric flow.

TABLE 2. Largest magnitudes for selected flow fields at 300 mb for day 2.

Quantity	Location	No drag	Ocean drag	Land drag
z' (m)	trough	−251	−238	−215
z' (m)	ridge	201	191	170
$\|v\|$ (m s^{-1})	above cold front	48.4	47.3	45.4
$\|v\|$ (m s^{-1})	downstream of ridge	43.8	42.2	39.7
$\|v_{ag}\|$ (m s^{-1})	trough	12.4	11.8	10.8
$\|v_{ag}\|$ (m s^{-1})	ridge	7.1	6.1	4.6
$\nabla\cdot v$ (10^{-5} s^{-1})	near cold front	0.64	0.66	0.81
$\nabla\cdot v$ (10^{-5} s^{-1})	upstream of ridge	1.26	0.98	0.78
$\nabla\cdot v$ (10^{-5} s^{-1})	trough	−1.61	−1.51	−1.41

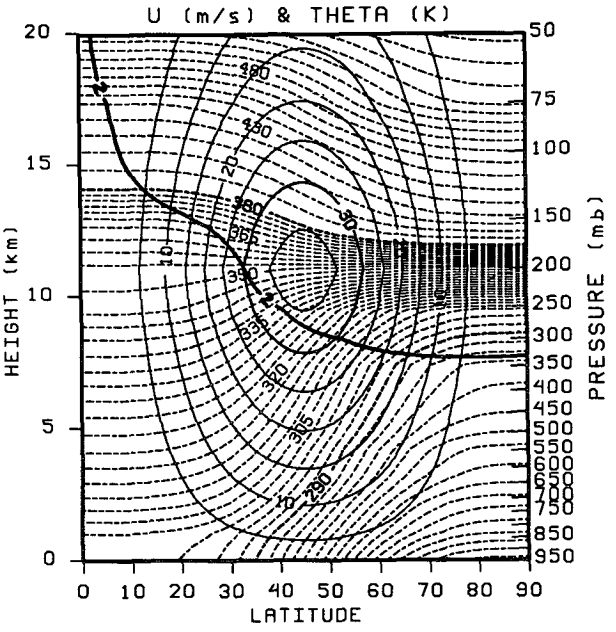

FIG. 21. As in Fig. 2 except for no drag D, ocean drag D, and land drag D.

7. Mature structure of cyclones

The simulations discussed so far did not produce a true spiral in the frontal zone around the surface low as in the fourth and final stage of the model of Shapiro and Keyser (1990). The cyclones decayed after day 3.5, and the bent-back fronts became diffuse. A repeat of the no-drag simulation (not shown) with the initial conditions shown in Fig. 2 and high horizontal resolution (0.6° latitude × 0.75° longitude) did not produce qualitatively new results. Significant differences in the structure of the bent-back front, however, are obtained in simulations performed with the high horizontal resolution and initial conditions that are slightly different from those shown in Fig. 2. The new initial conditions are shown in Fig. 21. The initial maximum wind speed in the upper troposphere is the same as in Fig. 2, but baroclinity is increased near the surface. For the new simulations, which we will refer to as no drag D, ocean drag D, and land drag D, the same drag coef-

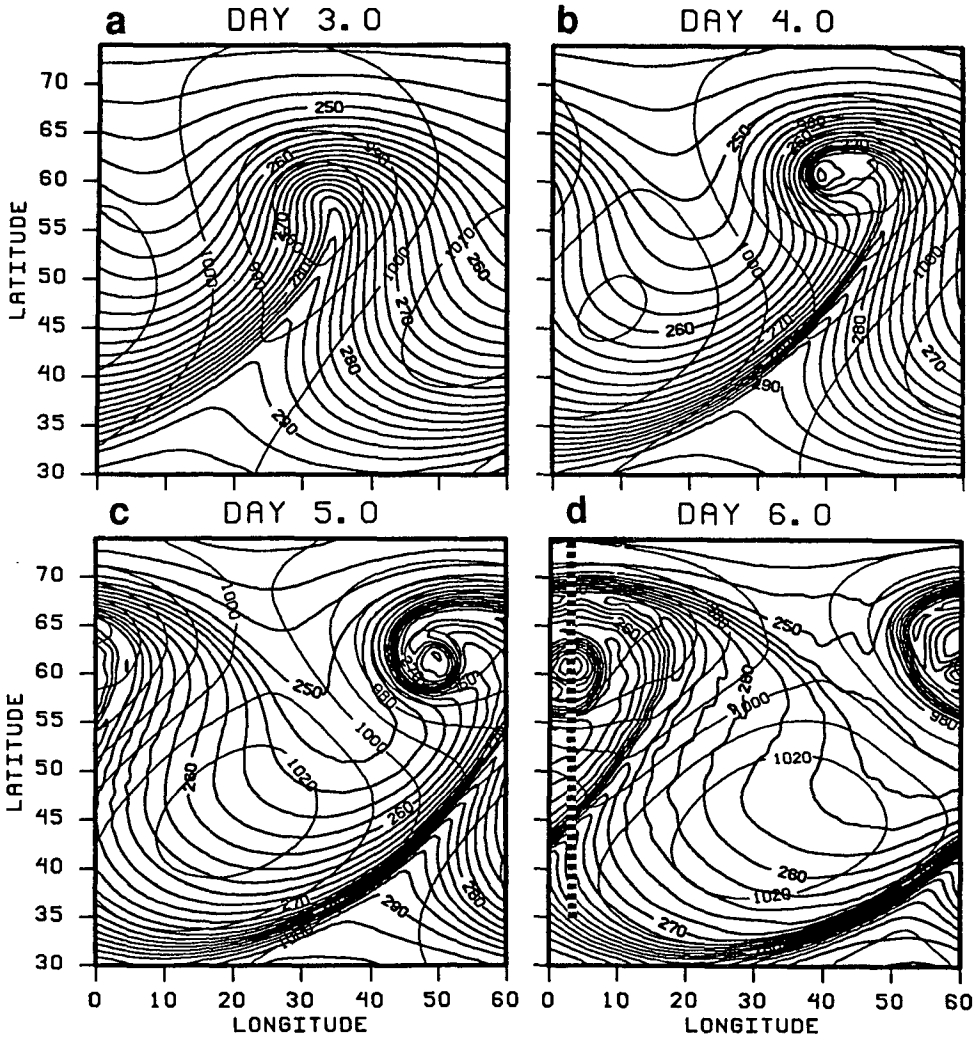

FIG. 22. Longitude–latitude contour plot of the model's lowest-level potential temperature (K, thick lines) and surface pressure (mb, thin lines) for ocean drag D at (a) day 3.0, (b) day 4.0, (c) day 5.0, and (d) day 6.0. Contour intervals are 2 K and 10 mb for potential temperature and surface pressure, respectively.

ficients as in no drag, ocean drag, and land drag, respectively, are used.

Figure 22 shows the time evolution of the sea level pressure and potential temperature at the lowest model level for ocean drag D. From a comparison of Fig. 22 with the last four panels of Fig. 4, it is apparent that the warm sector is narrower in ocean drag D than in ocean drag. During the evolution of the cyclone in ocean drag D, a bent-back front forms and increases in length as the cold front develops. A sharp warm front does not develop east of the northern edge of the cold front until the cold front is already mature. Eventually, the frontal zone spirals around the surface low similar to the structure shown in the last stage of the oceanic cyclone model of Shapiro and Keyser (1990). Spiraling cloud formations are often seen in satellite photographs of maritime cyclones [see, for example, Fig. 8b in Kuo and Reed (1988)]. Figure 23 shows a vertical section through the spiraling frontal zone along the dashed line in Fig. 22d. Note that the frontal zone is very shallow. A spiraling frontal zone is also produced in no drag D (not shown).

The lowest-level potential temperature and sea level pressure fields in land drag D are shown in Fig. 24. There is a slight enhancement of the temperature gradient just northwest of the surface low. An extended bent-back frontal zone, however, does not develop in this simulation. The cold frontogenesis proceeds at roughly the same rate as in ocean drag D.

In summary, the high horizontal resolution version of the model, starting with increased baroclinity in the lower troposphere, also produces bent-back fronts in

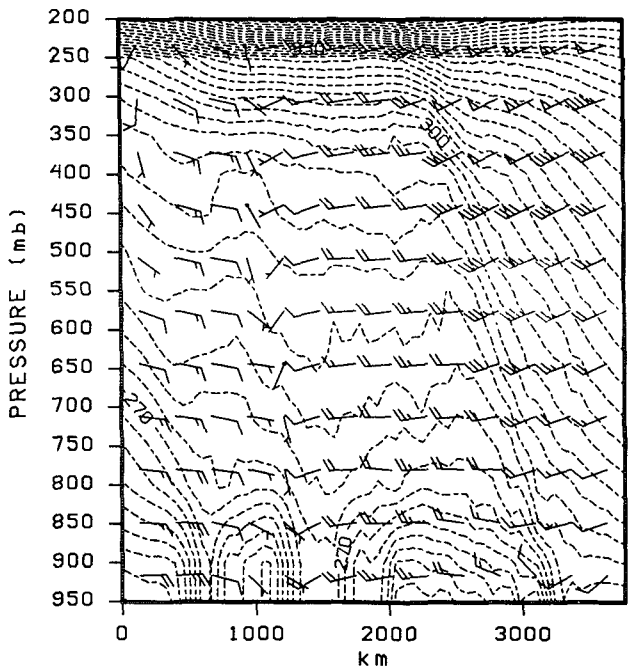

FIG. 23. Latitude–height plot at day 6 of potential temperature (K, solid lines) and horizontal velocity (wind barbs) in ocean drag D. The contour interval for potential temperature is 3 and 10 K, above and below 350 K, respectively. Flags, full wind barbs, and half-barbs, respectively, indicate speeds of 50, 10, and 5 m s^{-1}.

simulations with relatively small surface drag. Further, the cold fronts are relatively insensitive to surface drag. The simulations, however, are able to produce spiraling frontal zones that are not produced with lower horizontal resolutions.

8. Summary and conclusions

Recent developments in the theory and observations of fronts in connection with cyclogenesis have prompted renewed interest in the subject. Shapiro and Keyser (1990) present a modified conceptual model of oceanic cyclogenesis, which includes the formation of a bent-back front. Further, recent investigations of cyclogenesis over the oceans have shown special features suggestive of important influences from the underlying surface.

We have investigated frontogenesis during the simulated development of cyclones using a primitive equation model on the sphere, with physics reduced to surface drag given by the bulk aerodynamic formula, dry convective adjustment, and weak horizontal diffusion. The effect of surface drag on frontogenesis is examined in three simulations using a domain of a 60° sector of one hemisphere, horizontal resolution of 1.2° latitude × 1.5° longitude, and 21 levels in the vertical. The simulation referred to as no drag has a frictionless lower surface. The simulations referred to as ocean drag and land drag are performed with drag coefficients representative of an ocean surface and a continental surface, respectively.

Bent-back fronts develop in no drag and ocean drag. The initial development of the warm fronts is largely due to horizontal deformation, with divergence providing a smaller contribution. The bent-back structure develops as the warm fronts propagate westward in strong winds, and then southward on the western side of the surface lows. The local temperature gradient increase on the western edge of the frontal zone is due to intense horizontal advection, which overcomes weak frontolysis. The fracture of the poleward edge of the cold front near the triple point results from a gap between regions of intense warm and cold frontogenesis.

The surface drag and induced Ekman pumping weaken both the deepening of the surface lows and the corresponding growth in low-level wind speeds. The simulated warm fronts are quite sensitive to surface drag as the most intense warm front is in no drag, while a distinct warm front does not form in land drag. The sensitivity to surface drag is related to the nonuniformity of the reduction in wind speed. The low-level wind speed is considerably reduced by drag near the warm front and only slightly reduced near the cold front. This sensitivity appears to be enhanced by frictional retardation of a positive-feedback process at work for warm frontogenesis. This positive feedback involves deformation, vorticity, and the local vertical circulation. In no drag, and to a lesser extent, in ocean drag, strong, warm advection along the warm front is linked with strong ascent in the midtroposphere and horizontal convergence at the surface. The convergence increases deformation and vorticity. Consequently, deformation increases rapidly along the warm front. Surface drag weakens the warm advection and slows the intensification by positive feedback.

The intensity of simulated cold fronts, on the other hand, is not very sensitive to surface drag. Cold advection–type frontogenesis is associated with smaller upward vertical motions and does not appear to include the drag-sensitive positive feedback found along the warm fronts. Further, convergence increases along the cold front with increasing surface drag. The insensitivity of cold fronts to the value of the drag coefficient in our simulations is in agreement with the well-known prevalence of sharp cold fronts over sharp warm fronts in observations over the continents.

A frontal structure resembling that of the final stage of the model of Shapiro and Keyser (1990) is produced in simulations with small surface drag, doubled horizontal resolution (0.6° latitude × 0.75° longitude), and slightly enhanced low-level baroclinity in the initial conditions. In the mature stage of the simulated baroclinic wave, the bent-back front spirals around the surface low.

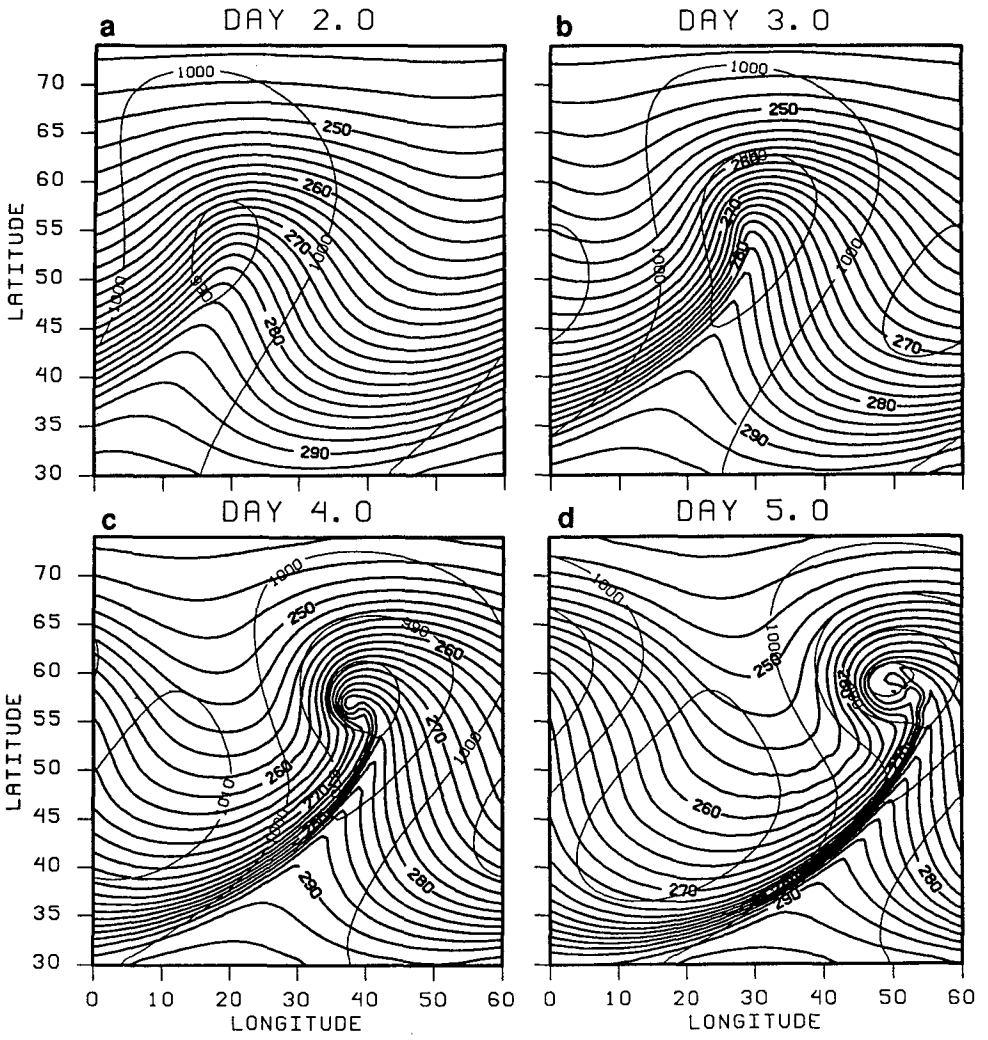

FIG. 24. As in Fig. 22 except land drag D at (a) day 2.0, (b) day 3.0, (c) day 4.0, and (d) day 5.0.

Our simulations have been performed in a nearly adiabatic framework and with a simple parameterization of surface friction. In spite of these idealizations, the results show features such as bent-back warm fronts and spiraling fronts. Consequently, our results contribute to clarify the precise role of adiabatic processes in frontogenesis and frontal evolution.

Acknowledgments. It is a pleasure to thank M. Shapiro, R. Reed, and C. Ma for stimulating discussions on this work. This research was supported by the NSF under Grants ATM 88-22729 and ATM 91-14850. The simulations were performed at the computer facility of NCAR.

REFERENCES

Arakawa, A., and V. R. Lamb, 1977: Computational design of the basic dynamical process of the UCLA general circulation model. *Methods in Comput. Phys.*, Academic Press, 173–275.

——, and ——, 1981: A potential enstrophy and energy conserving scheme for the shallow water equations. *Mon. Wea. Rev.*, **109,** 18–36.

Bannon, P. R., 1984: Effects of stratification on surface frontogenesis: Warm and cold fronts. *J. Atmos. Sci.*, **41,** 2021–2026.

Bergeron, T., 1937: On the physics of fronts. *Bull. Amer. Meteor. Soc.*, **18,** 265–275.

Bjerknes, J., 1919: On the structure of moving cyclones. *Geofys. Publ.*, **1,** 1–8.

——, and H. Solberg, 1921: Meteorological conditions for the formation of rain. *Geofys. Publ.*, **2,** 1–60.

Card, P. A., and A. Barcilon, 1982: The Charney stability problem with a lower Ekman layer. *J. Atmos. Sci.*, **39,** 2128–2137.

Davis, C. A., and K. A. Emanuel, 1988: Observational evidence for the influence of surface heat fluxes on rapid maritime cyclogenesis. *Mon. Wea. Rev.*, **116,** 2649–2659.

Eady, E. T., 1949: Long waves and cyclone waves. *Tellus*, **1,** 33–52.

Eliassen, A., 1962: On the vertical circulation in frontal zones. *Geofys. Publ.*, **24,** 147–160.

Emanuel, K. A., M. Fantini, and A. J. Thorpe, 1987: Baroclinic instability in an environment of small stability to slantwise moist convection. Part I: Two-dimensional models. *J. Atmos. Sci.*, **44,** 1559–1573.

Farrell, B., 1985: Transient growth of damped baroclinic waves. *J. Atmos. Sci.*, **42,** 2718–2727.

Fischer, G., 1977: The effect of various surface friction formulations on the development of cyclone waves and fronts. *Beitr. Phys. Atm.*, **50,** 71–77.

Gidel, L. T., 1978: Simulation of the differences and similarities of warm and cold surface frontogenesis. *J. Geophys. Res.*, **83,** 915–928.

Haltiner, G. J., and D. E. Caverly, 1965: The influence of friction on the growth and structure of baroclinic waves. *Quart. J. Roy. Meteor. Soc.*, **91,** 209–214.

Hines, K. M., and C. R. Mechoso, 1991: Frontogenesis processes in the middle and upper troposphere. *Mon. Wea. Rev.*, **119,** 1225–1241.

Hoskins, B. J., 1990: Theory of extratropical cyclones. *Extratropical Cyclones, The Erik Palmén Memorial Volume,* C. W. Newton and E. Holopainen, Eds., Amer. Meteor. Soc., 63–80.

——, and F. P. Bretherton, 1972: Atmospheric frontogenesis models: Mathematical formulation and solution. *J. Atmos. Sci.*, **29,** 11–37.

——, and N. V. West, 1979: Baroclinic waves and frontogenesis. Part II: Uniform potential vorticity jet flows—Cold and warm fronts. *J. Atmos. Sci.*, **36,** 1663–1680.

——, and W. A. Heckley, 1981: Cold and warm fronts in baroclinic waves. *Quart. J. Roy. Meteor. Soc.*, **107,** 79–90.

——, I. Draghici, and H. C. Davies, 1978: A new look at the omega-eqution. *Quart. J. Roy. Meteor. Soc.*, **104,** 31–38.

——, M. E. McIntyre, and A. W. Robertson, 1985: On the use and significance of isentropic potential vorticity maps. *Quart. J. Roy. Meteor. Soc.*, **111,** 877–946.

Hsie, E.-Y., R. A. Anthes, and D. Keyser, 1984: Numerical simulation of frontogenesis in a moist atmosphere. *J. Atmos. Sci.*, **41,** 2581–2594.

Keyser, D., and R. A. Anthes, 1982: The influence of planetary boundary layer physics on frontal structure in the Hoskins–Bretherton horizontal shear model. *J. Atmos. Sci.*, **39,** 1783–1802.

——, and M. J. Pecnick, 1987: The effect of along-front temperature variation in a two-dimensional primitive equation model of surface frontogenesis. *J. Atmos. Sci.*, **44,** 577–604.

Kuo, Y.-H., and R. J. Reed, 1988: Numerical simulation of an explosively deepening cyclone in the eastern Pacific. *Mon. Wea. Rev.*, **116,** 2081–2105.

——, and S. Low-Nam, 1990: Prediction of nine explosive cyclones over the western Atlantic Ocean with a regional model. *Mon. Wea. Rev.*, **118,** 3–25.

——, R. J. Reed, and S. Low-Nam, 1991a: Effects of surface energy fluxes during the early development and rapid intensification stages of seven explosive cyclones in the western Atlantic. *Mon. Wea. Rev.*, **119,** 457–476.

——, M. A. Shapiro, and E. G. Donall, 1991b: The interaction between baroclinic and diabatic processes in a numerical simulation of a rapidly intensifying extratropical marine cyclone. *Mon. Wea. Rev.*, **119,** 368–384.

——, R. J. Reed, and S. Low-Nam, 1992: Thermal structure and airflow in a model simulation of an occluded marine cyclone. *Mon. Wea. Rev.*, **120,** 2280–2297.

Levy, G., 1989: Surface dynamics of observed maritime fronts. *J. Atmos. Sci.*, **46,** 1219–1232.

Lorenz, E. N., 1960: Energy and numerical weather prediction. *Tellus,* **12,** 364–373.

Manabe, S., J. L. Holloway, Jr., and H. M. Stone, 1970: Simulated climatology of a general circulation model with a hydrologic cycle. III: Effects of increased horizontal computational resolution. *Mon. Wea. Rev.*, **98,** 175–212.

Mass, C. F., 1991: Synoptic frontal analysis: Time for a reassessment? *Bull. Amer. Meteor. Soc.*, **72,** 348–363.

Miller, J. E., 1948: On the concept of frontogenesis. *J. Meteor.*, **5,** 169–171.

Mudrick, S. E., 1974: A numerical study of frontogenesis. *J. Atmos. Sci.*, **31,** 869–892.

——, 1978: A further test of a scale-dependent filter for use in finite-difference modeling. *Mon. Wea. Rev.*, **106,** 1205–1211.

Mullen, S. L., and D. P. Baumhefner, 1988: The sensitivity of numerical simulations of explosive oceanic cyclogenesis to changes in physical parameterizations. *Mon. Wea. Rev.*, **116,** 2289–2329.

Neiman, P. J., M. A. Shapiro, E. G. Donall, and C. W. Kreitzberg, 1990: Diabatic modification of an extratropical marine cyclone warm sector by cold underlying water. *Mon. Wea. Rev.*, **118,** 1576–1590.

Ogura, Y., and D. Portis, 1982: Structure of the cold front observed in SESAME-AVE III and its comparison with the Hoskins–Bretherton frontogenesis model. *J. Atmos. Sci.*, **39,** 2773–2792.

Oort, A. H., 1983: Global atmospheric circulation statistics, 1958–1973. NOAA Prof. Pap. 14, 180 pp. [NTIS PB84-129717.]

Orlanski, I., B. B. Ross, L. Palinsky, and R. Shaginaw, 1985: Advances in the theory of atmospheric fronts. *Adv. in Geophys.*, **28B,** 223–252.

Sanders, F., 1955: An investigation of the structure and dynamics of an intense surface frontal zone. *J. Meteor.*, **12,** 542–552.

——, and J. R. Gyakum, 1980: Synoptic–dynamic climatology of the "bomb". *Mon. Wea. Rev.*, **108,** 1589–1606.

Schär, C. J., 1989: Dynamische Aspekte der aussertropischen Zyklogenese, Theorie und numerische Simulation im Limit der balancierten Strömungssysteme. Disseration Nr. 8845 der Eidgenossischen Technischen Hochschule, Zurich, 241 pp.

Shapiro, M. A., and D. Keyser, 1990: Fronts, jet streams, and the tropopause. *Extratropical Cyclones, The Erik Palmén Memorial Volume,* C. W. Newton and E. Holopainen, Eds., Amer. Meteor. Soc., 167–191.

Takayabu, I., 1986: Roles of the horizontal advection on the formation of surface fronts and on the occlusion of a cyclone developing in the baroclinic westerly jet. *J. Meteor. Soc. Japan,* **64,** 329–345.

Trenberth, K. E., 1978: On the interpretation of the diagnostic quasi-geostrophic omega equation. *Mon. Wea. Rev.*, **106,** 131–137.

Valdes, P. J., and B. J. Hoskins, 1988: Baroclinic instability of the zonally averaged flow with boundary layer damping. *J. Atmos. Sci.*, **45,** 1584–1593.

Wallace, J. M., and P. V. Hobbs, 1977: *Atmospheric Science: An Introductory Survey.* Academic Press. 467 pp.

Williams, R. T., 1974: Numerical simulation of steady-state fronts. *J. Atmos. Sci.*, **31,** 1286–1296.

——, L. C. Chou, and C. J. Cornelius, 1981: Effects of condensation and surface motion on the structure of steady-state fronts. *J. Atmos. Sci.*, **38,** 2365–2376.